Examining the sensitivity of ECMWF IFS weather forecasts to sea-ice coupling for the summer-time Arctic and cyclones

Croad, H. L. ORCID: https://orcid.org/0000-0002-5124-4860, Keeley, S. P. E. ORCID: https://orcid.org/0000-0002-8046-765X, Methven, J. ORCID: https://orcid.org/0000-0002-7636-6872, Harvey, B. ORCID: https://orcid.org/0000-0002-6510-8181 and Volonté, A. ORCID: https://orcid.org/0000-0003-0278-952X (2024) Examining the sensitivity of ECMWF IFS weather forecasts to sea-ice coupling for the summer-time Arctic and cyclones. Quarterly Journal of the Royal Meteorological Society. ISSN 1477-870X doi: https://doi.org/10.1002/qj.4899 Available at https://centaur.reading.ac.uk/120066/

Received: 5 June 2024 | Revised: 14 October 2024 | Accepted: 28 October 2024

DOI: 10.1002/qj.4899

Quarterly Journal of the Royal Meteorological Society RMetS

RESEARCH ARTICLE

Examining the sensitivity of ECMWF IFS weather forecasts to sea-ice coupling for the summer-time Arctic and cyclones

Hannah L. Croad[1] | **Sarah P. E. Keeley**[2] | **John Methven**[1] | **Ben Harvey**[1,3] | **Ambrogio Volonté**[1,3]

[1]Department of Meteorology, University of Reading, Reading, UK

[2]European Centre for Medium-Range Weather Forecasts (ECMWF), Reading, UK

[3]National Centre for Atmospheric Science (NCAS), University of Reading, Reading, UK

Correspondence
Hannah L. Croad, Department of Meteorology, University of Reading, Reading, RG6 6ET, UK.
Email: hannah.croad@reading.ac.uk

Funding information
SCENARIO NERC Doctoral Training Partnership, Grant/Award Number: NE/S007261/1; NERC standard grant (Arctic Summer-time Cyclones: Dynamics and Sea-Ice Interaction), Grant/Award Number: NE/T006773/1; National Centre for Atmospheric Science, Grant/Award Number: R8/H12/83

Abstract

In recent years there has been an advance towards coupled Earth-system models for weather forecasting. For example, the European Centre for Medium-Range Weather Forecasts now implements ocean–ice coupling with dynamic sea ice in the Integrated Forecasting System (IFS) at all time ranges. This has the potential to improve weather forecasts in the polar regions, where sea ice influences the overlying atmosphere directly by turbulent exchange, especially in the rapidly warming summer-time Arctic where thinner and more mobile ice is susceptible to rapid change. In this study, we investigate the sensitivity of IFS (cycle 47r1) weather forecasts to sea-ice coupling representation in the summer-time Arctic by comparing three sets of forecasts that are coupled with (i) dynamic sea ice in operational configuration, (ii) static sea ice, and (iii) dynamic sea ice with additional thermodynamic (surface temperature and albedo) coupling. It is found that dynamic sea ice improves predictions of sea ice and the ice edge compared with persistence, especially in the vicinity of Arctic cyclones. The dynamic sea-ice forecasts exhibit lower near-surface temperatures (up to 0.5 °C) compared with static sea-ice forecasts where ice loss has occurred, and differences in near-surface winds of up to 0.5 m s^{-1}, consistent with changing surface roughness over the marginal ice zone. The forecasts with additional thermodynamic coupling have near-surface temperatures that are up to 1 °C cooler over ice than the operational configuration (correcting a known warm bias), consistent with a more stable boundary layer (BL) and weaker near-surface winds. The influence of sea-ice coupling above the BL is small, with differences in cyclone forecasts being smaller than the spread of the operational ensemble. This study highlights the influence of ocean–ice coupling in weather forecasts for the summer-time Arctic, and the potential gains from improving its representation.

KEYWORDS

Arctic cyclones, boundary layer, coupled numerical weather prediction, coupled sea ice, marginal ice zone, sea ice, summer-time Arctic

1 | INTRODUCTION

Since 1979 the Arctic has warmed nearly four times faster than the global average (Rantanen *et al.*, 2022), and the associated rapid decline of sea ice (e.g., Meier & Stroeve, 2022) is driving increasing interest in socio-economic activities in the Arctic, including resource extraction, shipping, and tourism (Stephenson *et al.*, 2011). Hence, there is a growing demand for accurate forecasts of Arctic weather and sea ice on a range of timescales to support human activity in the region.

In recent years dynamical forecast systems for sea-ice predictions on seasonal timescales and longer have been established (Guemas *et al.*, 2016), exhibiting some predictive skill for pan-Arctic (and regional) sea-ice extent and volume out to a few months ahead (e.g., Bushuk *et al.*, 2019). Predictability at these timescales is beneficial for forecasting the sea-ice state itself, but also for capturing important feedbacks on atmospheric circulation and precipitation (Balmaseda *et al.*, 2010; Screen, 2013). For predictions on subseasonal timescales, Zampieri *et al.* (2018) demonstrated a wide range in skill across operational forecasting systems with coupled sea ice, with the best showing predictive skill out to 1.5 months. The need for coupled sea ice on shorter timescales relevant to weather forecasts (1–10 days) has received less attention, although Mohammadi-Aragh *et al.* (2018) indicated some potential in this regard.

Until recently, operational numerical weather prediction (NWP) systems have typically kept sea-ice fields fixed for weather forecasts, based on the assumption that changes in sea ice are slow and that models would not be able to beat a persistence forecast. However, Keeley and Mogensen (2018) demonstrated that static sea ice is a poor assumption for NWP, especially in summer, with on average more than 5% of the Arctic ice field exhibiting significant changes over five-day periods during June–November 2017. One way in which this may be realised is through very rapid ice-loss events (VRILEs), extreme reductions in sea-ice extent on a timescale of days, which are associated with anomalous synoptic activity (e.g., Wang *et al.*, 2020). For example, an extremely strong Arctic cyclone in August 2012 (Simmonds & Rudeva, 2012) was associated with substantial ice melt (Stern *et al.*, 2020) and ultimately reduced ice extent that constituted a VRILE (McGraw *et al.*, 2022).

The presence of sea ice has a strong influence on the atmospheric boundary layer (BL; Notz, 2012). The marginal ice zone (MIZ), a heterogeneous band of fragmented ice floes separating the ice-free ocean and main ice pack, is associated with gradients in roughness, temperature, and humidity that result in turbulent exchange of momentum, heat, and moisture. Momentum fluxes and surface roughness peak in the MIZ at sea-ice fraction (SIF) values of 0.5–0.8 (Elvidge *et al.*, 2016; Lüpkes & Birnbaum, 2005), primarily due to form drag over ice-floe edges. Off-ice flow (e.g., during cold-air outbreaks) is typically associated with cold air moving over the warm ocean surface, with upward surface sensible and latent heat fluxes and a transition from a stable or neutral BL to one that is unstable (e.g., Renfrew & Moore, 1999). In contrast, the BL is cooled and dried during on-ice flow, such as during warm-air intrusions (e.g., Pithan *et al.*, 2018). In recent years, physical parametrisations that depend on SIF for surface momentum, heat, and moisture fluxes have been shown to improve representation of surface turbulent exchange in NWP (Elvidge *et al.*, 2021, 2023; Renfrew *et al.*, 2019). However, capturing the location and geometry of the ice edge correctly is also important, due to the strong influence of this in the development of the downstream BL (e.g., Liu *et al.*, 2006; Spensberger & Spengler, 2021). Hence, coupled NWP models with dynamic sea ice that can capture rapid changes in sea ice (e.g., during VRILEs) have the potential to predict these downstream impacts and improve weather forecasts in the Arctic.

Accordingly, in recent years there have been ongoing efforts towards coupled ocean and ice components in NWP models. Building on positive results from regional coupled NWP systems (e.g., Pellerin *et al.*, 2004; Smith *et al.*, 2013), operational centres including Environment and Climate Change Canada (ECCC; e.g., Smith *et al.*, 2018; Peterson *et al.*, 2022), the European Centre for Medium-Range Weather Forecasts (ECMWF; e.g., Keeley & Mogensen, 2018), and the United States Naval Research Laboratory (NRL; Barton *et al.*, 2021) have now implemented atmosphere–ocean–ice coupling in their operational global weather forecasting systems. ECMWF, the focus of this study, implemented atmosphere–ocean–ice coupling in the Integrated Forecasting System (IFS) in their ensemble prediction system (EPS) in November 2016, and then in their high-resolution deterministic forecasts in June 2018 (Keeley & Mogensen, 2018). This is facilitated by coupling the IFS to a dynamic ocean model (Nucleus for European Modelling for the Ocean; NEMO), which incorporates a dynamic–thermodynamic sea-ice model (Louvain-la-Neuve version 2; LIM2). Focusing on a winter evaluation period, Day *et al.* (2022) demonstrated that this atmosphere–ocean–ice coupling in the IFS generally improves medium-range forecasts of the sea-ice edge and the downstream BL in the Arctic, compared with the previous uncoupled system. However, some localised regions see a degradation in forecast skill, demonstrating that challenges with the atmosphere–ocean–ice coupling remain.

No corresponding evaluation of this coupled system has been performed in summer, when the Arctic is most accessible and therefore there is the greatest demand for weather forecasts to support human activity. Surface

turbulent exchange near the ice edge in summer differs from that in winter, with typically much smaller turbulent heat fluxes due to the atmosphere and ocean having more similar temperatures than in winter (when turbulent heat fluxes can be of the order of 100 W m^{-2} during off-ice flow: e.g., Elvidge *et al.*, 2021; Renfrew & Moore, 1999). Instead, surface exchange over ice might be dominated by surface drag and turbulent momentum fluxes. The summer-time Arctic is becoming increasingly dominated by the MIZ (Rolph *et al.*, 2020; Strong & Rigor, 2013), which, due to more mobile and rough ice, may enhance surface exchange and interactions with Arctic weather systems. In particular, Arctic cyclones are associated with strong winds and ocean waves that have large impacts on the thinning sea-ice cover in summer (e.g., Asplin *et al.*, 2012; Peng *et al.*, 2021). How this interaction with sea ice feeds back on the cyclones is less clear, and has not previously been examined in NWP models with coupled sea ice.

In this study we build on the work of Day *et al.* (2022) by examining the sensitivity of IFS forecasts in the summer-time Arctic (with a focus on cyclones) to sea-ice coupling representation. With regards to surface drag over ice in the IFS, the surface roughness is represented via a roughness length that is dependent on SIF (ECMWF, 2020). However, ocean wave propagation is suppressed in the model for SIF greater than 0.3 (ECMWF, 2023b), which is likely a key process for surface drag in the MIZ. Furthermore, comparison with observations from the Arctic Ocean 2018 expedition highlights that surface and near-surface temperatures over sea ice in the IFS are too warm during summer, with biases of +0.5 °C and +0.5–1.0 °C, respectively, such that both are above zero in spite of ongoing melt (Tjernström *et al.*, 2021). In the current ECMWF operational setup, the only sea-ice variable coupled to the atmosphere is SIF. The surface temperature over sea ice is not coupled, with the surface energy balance calculated on the sea-ice tile in the land-surface scheme (Keeley & Mogensen, 2018). Using a more comprehensive thermodynamic coupling over sea ice would aim to produce more physical solutions and improved forecasts.

In this study we examine and compare three sets of 10-day forecast experiments run with the IFS that differ only in their sea-ice coupling configurations, starting daily at 0000 UTC during July 20–August 25, 2020. The 2020 summer was selected as the period of interest due to the regular passage of Arctic cyclones; Croad *et al.* (2023a) identified 52 Arctic cyclones during the extended summer season (May–September), compared with an average of ∼39 cyclones per summer during 1979–2021 (Croad *et al.*, 2023b). The dates selected were chosen as a period with rapid sea-ice loss, and to capture the occurrence of a known extreme cyclone in July that was examined in Croad *et al.* (2023a). The three sets of IFS forecast experiments to be compared are coupled with (i) "dynamic sea ice", in operational configuration (henceforth C_{oper}), (ii) "static sea ice", where the sea ice cannot evolve throughout the forecast, as was operational prior to November 2016 (henceforth C_{static}), and (iii) dynamic sea ice with additional "thermodynamic coupling" (henceforth C_{thermo}) over sea ice in an experimental setup. We aim to answer the following questions.

1. Where does dynamic coupling with the ocean–sea-ice model have the greatest impact on sea-ice forecasts?
2. How does dynamic sea ice impact the forecast BL compared with static sea ice?
3. How does additional thermodynamic coupling impact the forecast BL compared with dynamic sea ice alone?
4. What is the impact of sea-ice coupling on Arctic cyclone forecasts?

The article is structured as follows. The methodology is described in Section 2, including details of the sea-ice coupling configuration in each set of IFS forecast experiments. The results are presented in Section 3, where forecasts of sea ice, BL quantities, and Arctic cyclones are evaluated. The study is concluded in Section 4.

2 | METHODOLOGY

2.1 | Experiments

The three sets of forecast experiments were run using IFS model cycle 47r1 (Cy47r1), which employs a spectral model with an octahedral reduced Gaussian grid $T_{CO}639$ (horizontal resolution ∼18 km) and 91 terrain-following hybrid pressure levels up to 0.01 hPa. This is the same setup as the ensemble members in the ECMWF's operational EPS for the cycle, although the forecasts used in this study are deterministic (i.e., a single control member is run for each experiment at each start time). In all three sets of forecasts, the ocean and sea-ice fields are initialised from the ECMWF OCEAN5 analysis (Zuo *et al.*, 2019; see more details in section 2.2) and the atmosphere is initialised from the ECMWF operational control analysis. The experiments all have the same ocean–atmosphere coupling as that in the operational EPS, with sea-surface temperatures (SSTs) being fully coupled in the tropics but only partially coupled in the extratropics for the first four days (ECMWF, 2024). Roughness lengths for momentum, heat, and moisture are prescribed in each experiment as in the operational configuration of IFS Cy47r1 (ECMWF, 2020). Over sea ice, the roughness length for momentum depends

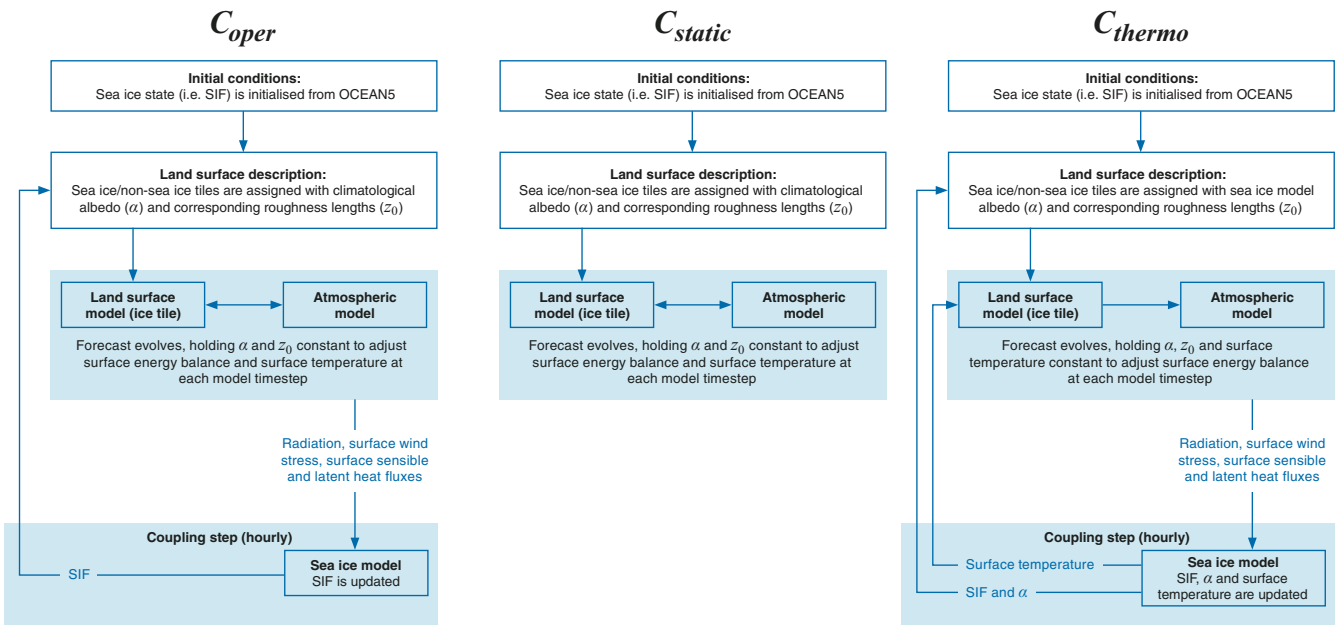

FIGURE 1 A schematic diagram describing the coupled sea-ice configuration in the three experiments: (left) C_{oper}, (middle) C_{static}, and (right) C_{thermo}.

on SIF (with a maximum value at 0.5 SIF), whilst the scalar roughness lengths are constants. For the fields shown in this study, we use six-hourly forecast data interpolated to a 0.25° regular latitude–longitude grid.

Figure 1 describes the sea-ice coupling in the three sets of forecast experiments. In the first set of forecasts, C_{oper}, the IFS atmospheric model is coupled to the ocean–sea-ice (NEMO-LIM2) models consistent with the operational implementation of Cy47r1. The only sea-ice variable coupled to the atmosphere is SIF (ECMWF, 2020). A uniform climatological sea-ice albedo value (assuming bare ice in summer) from Ebert and Curry (1993) is used rather than using the albedo from the sea-ice model, which can be too high in summer due to the lack of melt-pond processes in the LIM2 model (Keeley & Mogensen, 2018). Coupling between the atmosphere and ocean–sea-ice models occurs once per hour, rather than every atmospheric model time step. Hence, SIF is updated every coupling step (informing the surface albedo and roughness lengths for momentum, heat, and moisture), with the sea-ice tile in the surface scheme being used to adjust the surface energy balance and surface temperature on faster timescales (left panel in Figure 1).

The second set of forecasts, C_{static}, is identical to C_{oper} except that the sea-ice field is persisted from the start of the forecast (middle panel in Figure 1).

The third set of forecasts, C_{thermo}, is an experimental setup that is identical to C_{oper} except that the sea ice is also coupled thermodynamically, with albedo and surface temperature from the LIM2 sea-ice model being coupled to the atmosphere as well as SIF (similar to the "Tight" coupling experiment in Arduini *et al.*, 2022, but with albedo coupled also). In this setup, the surface temperature and albedo over ice in the atmospheric model are fixed to those from the LIM2 sea-ice model (with the thermodynamic calculations on the sea-ice tile in the surface scheme being disabled). This surface temperature is physically consistent with the surface energy balance that is calculated in LIM2 within each coupling step, including the phase transitions of sea ice and snow. However, the system is still not fully coupled, with the surface temperature over ice being held constant for each hourly coupling step (right panel in Figure 1) so that fluctuations on faster timescales are not possible. There is also the potential for surface albedos that are too high, as the LIM2 implementation does not represent melt ponds. Note that the forecasts have the same initial conditions as the other experiments (i.e., analyses produced by a data assimilation system in which there is no thermodynamic coupling with the sea-ice model). Hence, the thermodynamic coupling leads to an imbalance between the ocean–sea-ice model and atmosphere at the first coupling step, driving rapid adjustments in surface fluxes to establish a new thermodynamical balance. This initialisation shock could accelerate the development of errors in the forecast. Hence, this thermodynamic coupling is not implemented operationally, but these experiments explore the potential benefits of doing so.

2.2 | Evaluation

This study is focused primarily on comparing the different forecast experiments and understanding the model response to changing sea-ice coupling representation, rather than verification against a truth dataset. This is because our knowledge of the true atmospheric state is limited over ice, with sparse in situ observations (in space and time) and reanalysis products having known deficiencies (e.g., Graham *et al.*, 2017; Wesslén *et al.*, 2014). For example, ERA5 reanalysis has a known warm bias over sea ice (Wang *et al.*, 2019). Evaluation of reanalyses over ice is a complicated matter in its own right (beyond the scope of this article), so here we focus on investigating model sensitivity to sea-ice coupling.

That being said, a brief evaluation of sea-ice forecasts from the experiments is performed against the OCEAN5 analysis used to initialise forecasts at the same valid time. OCEAN5 estimates the state of the sea ice and ocean using the same ocean–sea-ice model configuration as C_{oper} and a 3D variational assimilation system, assimilating Operational Sea Surface Temperature and Sea Ice Analysis (OSTIA: Donlon *et al.*, 2012) gridded sea-ice concentrations and SSTs (more precisely, it relaxes towards them) in addition to other ocean observations (see Zuo *et al.*, 2019 for more details).

Although the atmospheric forecasts are not compared with a "truth" dataset, we benchmark the differences between the experiments to the spread of the operational forecasts from the EPS ensemble members initialised at the same time. The EPS is comprised of 51 ensemble members with the same setup as C_{oper}, except that perturbations are applied to the ocean and atmospheric initial conditions, and atmospheric physical parametrisation tendencies. This accounts for forecast uncertainty related to the initial conditions and the forecast model itself, in terms of subgrid-scale phenomena that are not captured in the formulation of physical parametrisations.

2.3 | Cyclone tracks

Cyclone tracks are identified in ERA5, the fifth-generation ECMWF reanalysis dataset (Hersbach *et al.*, 2017, 2020), produced using the ECMWF's Integrated Forecasting System (Cy41r2). The model has spectral truncation T_L639 (~31 km resolution at the Equator) and 137 terrain-following hybrid-pressure levels from the surface to 0.01 hPa.

Arctic cyclone tracks are obtained from ERA5 reanalysis using the TRACK algorithm (Hodges, 1994, 1995, 2021). The algorithm is employed on one-hourly spectrally truncated (T5–63; removing total wavenumbers less than 5 and more than 63) 850-hPa relative vorticity. Maxima exceeding 10^{-5} s^{-1} are identified, initialized into a set of tracks using a nearest-neighbour search with a maximum great-circle displacement distance of 2° in a time step, and are subsequently refined by minimizing a cost function for track smoothness. Arctic cyclones are identified as those tracks where filtered 850-hPa relative vorticity exceeds 8×10^{-5} s^{-1} for at least 12 hours whilst located north of 70°N. Cyclone tracks are presented at six-hourly intervals interpolated onto a 0.25° regular latitude–longitude grid. The spatial track density of cyclones was computed with cosine-shaped kernels on a polar domain (500-km bandwidth) using the scikit-learn Python library (Pedregosa *et al.*, 2011).

3 | RESULTS

3.1 | Forecasts of sea ice

In this section, the extent to which dynamic coupling impacts sea-ice forecasts is examined, by comparing the C_{oper} and C_{static} forecasts (note that C_{oper} and C_{thermo} forecasts have virtually identical sea-ice fields; Section 3.2). In Figure 2, maps of the differences in SIF between C_{oper} and C_{static}, averaged over all forecast start dates, are presented at 3-day (Figure 2a) and 10-day (Figure 2b) lead times. The differences in SIF are largely negative, reflecting a loss of sea ice in C_{oper} (as would be expected in this summer melting period) that is not possible in C_{static}. Here we focus on two regions in which large differences occur. The first region is to the north of the Bering Strait, which shall henceforth be referred to as the "Pacific" sector (demarcated by the purple box), with reduced SIF in C_{oper} over a broad area. The second region is to the north of the Greenland–Barents–Kara Seas region, and shall henceforth be referred to as the "Eurasian" sector (demarcated by the green box). In this region the reduced SIF in C_{oper} is limited to a relatively thin region close to the ice edge.

The Pacific sector experiences the highest density of cyclone activity during this period, with four Arctic cyclone tracks (Figure 2c) contributing to a high track density (Figure 2d) over the sea ice in this region. Furthermore, there is considerable cyclone activity in the Greenland–Barents–Kara Seas region (Figure 2c,d), which would likely be associated with across-ice edge flow to the north in the Eurasian sector. Hence, the largest differences in SIF forecasts from C_{oper} and C_{static} (Figure 2a,b) occur in the vicinity of Arctic cyclones. These systems are associated with strong winds and/or warm intrusions that can result in rapid losses of sea ice. The sea ice in the C_{oper} forecasts can respond to these atmospheric forcings, but not that in C_{static}.

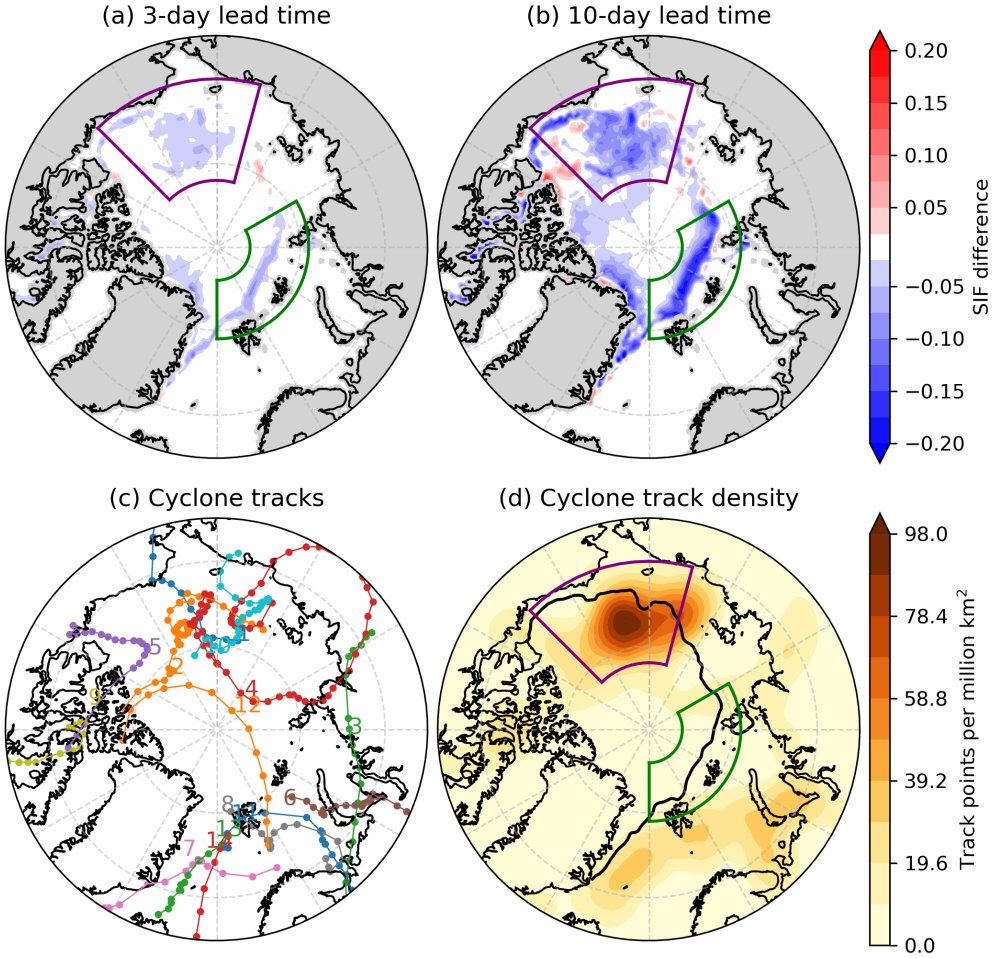

FIGURE 2 The difference ($C_{oper} - C_{static}$) in sea-ice fraction (SIF), averaged over all forecast start dates, at (a) 3-day and (b) 10-day lead times. The six-hourly tracks of Arctic cyclones identified in ERA5 reanalysis during the study period are presented as (c) individual trajectories and (d) a feature track density map using spherical cosine kernels with bandwidth 500 km (shading; track points per million km^2), with the composite mean sea-ice edge (black contour; 0.15 SIF) overlaid. The regions marked with purple and green borders are the Pacific and Eurasian sectors, respectively.

Forecasts of the sea-ice area (SIA sea-ice extent weighted by grid-box SIF) from C_{oper} and C_{static} are compared with that from the ECMWF operational OCEAN5 analysis at the same valid time in Figure 3. Note that in this study sea-ice grid points are those with SIF> 0.15, whilst all non-land grid points with SIF< 0.15 are considered to be ocean. The operational analysis and the C_{oper} forecasts show a consistent reduction in SIA with time, as would be expected in this late summer melting period. Figure 3 highlights that the C_{oper} forecasts produce much improved SIA predictions compared with C_{static}, with the root-mean-square errors (relative to the operational analysis) reduced by approximately half in all sectors. This highlights how poor an assumption static sea ice can be on weather timescales during the summer. However, the reduction in SIA from the C_{oper} forecasts is typically underestimated compared with the operational analysis over the whole Arctic (Figure 3a). The SIA loss in C_{oper} is particularly underestimated in the Pacific sector (Figure 3b). It is known that the LIM2 sea-ice model tends to melt sea ice too slowly, particularly where the analysis overestimates sea-ice thickness (ECMWF, 2023a), since heat transfer within the ice model assumes a constant thickness of 1.5 m (ECMWF, 2020). Previous studies have noted that sea-ice thickness is overestimated in the ECMWF model in the Pacific sector (Balan-Sarojini *et al.*, 2021; Xiu *et al.*, 2022), which would be consistent with the underestimation of the ice-loss rate we have identified in this region. Furthermore, the forecasts do not represent ocean wave propagation into the sea ice, which is an important process in the breakup of sea ice in reality. In contrast, the SIA forecasts from C_{oper} are more similar to the operational analysis in the Eurasian sector, although the SIA loss is occasionally overestimated (Figure 3c). This is consistent with the underestimation of sea-ice thickness in the ECMWF model in the Eurasian sector (Balan-Sarojini *et al.*, 2021; Xiu *et al.*, 2022).

A more user-relevant verification metric for sea ice, given the dependence of the downstream BL on the location and geometry of the ice edge, is the integrated ice-edge error (IIEE; Goessling *et al.*, 2016). The IIEE of a forecast is the sum of the areas of sea ice that are overestimated and underestimated compared with the truth, here the ECMWF operational OCEAN5 analysis. In Figure 4 it is seen that the IIEE in C_{oper} is reduced compared with C_{static} at all lead times for the Pan-Arctic (Figure 4a), and in the Pacific (Figure 4b) and Eurasian (Figure 4c) sectors. Consistent with the comparison of SIA forecasts in Figure 3,

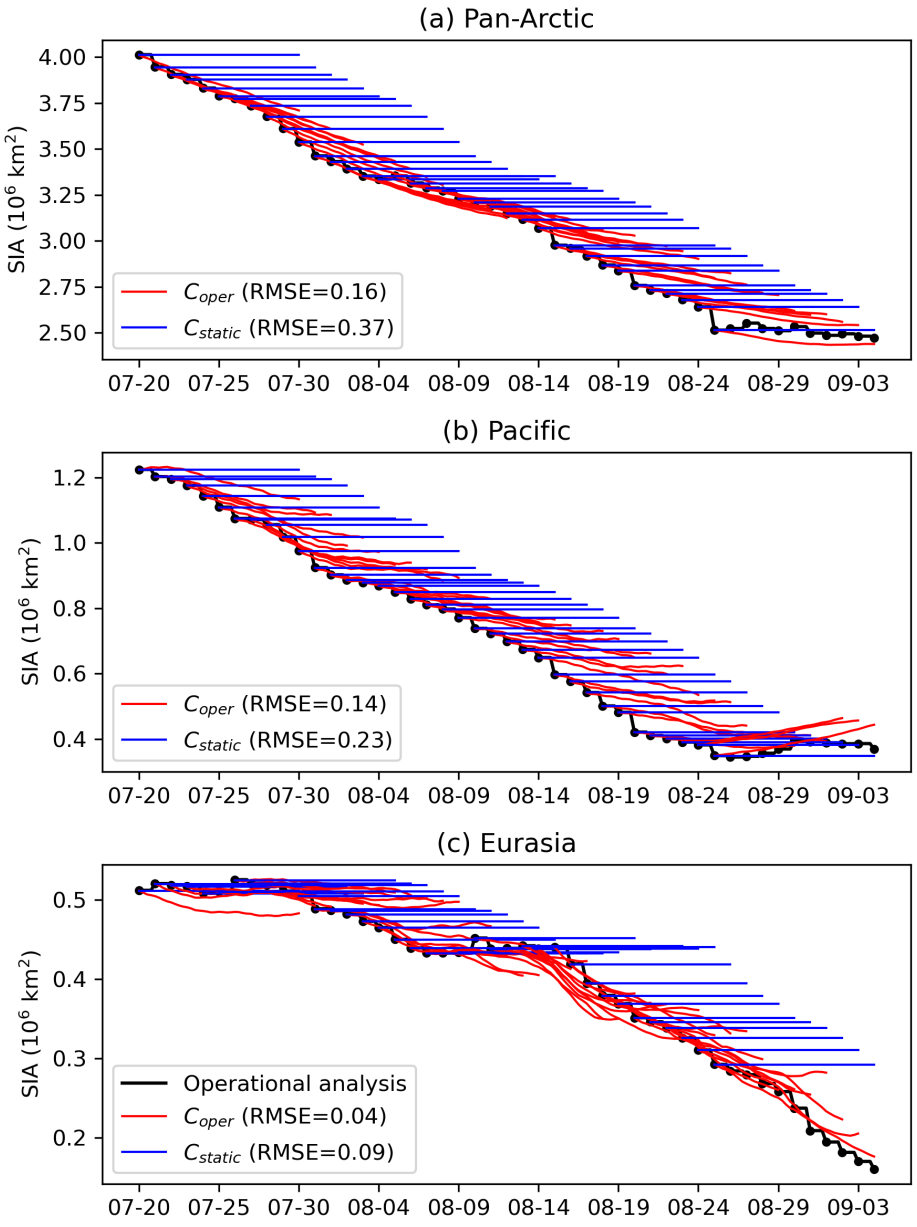

FIGURE 3 Time series of sea-ice area (SIA) from the ECMWF operational analysis (black lines) for the (a) Pan-Arctic, (b) Pacific, and (c) Eurasian sectors, and 10-day forecasts from C_{oper} (red lines) and C_{static} (blue lines) starting at 0000 UTC daily (indicated by black markers). The root-mean-square error (RMSE) for C_{oper} and C_{static} relative to the operational analysis at day 10 is presented in the legend for each region.

the reduction in IIEE in C_{oper} compared with C_{static} is more marked in the Eurasian sector (Figure 4c) than the Pacific sector (Figure 4b, where in general the SIF is reduced but the ice cover is not completely removed). In all regions, the rate of growth in IIEE in C_{oper} is particularly reduced compared with C_{static} in the first five days of the forecasts. During days 5–10, the lines in Figure 4 are roughly parallel, indicating that the rate of growth of IIEE in both experiments is similar.

The IIEE can also be decomposed into the sum of the absolute extent error (AEE) and misplacement error (ME). The AEE is the absolute difference between the overestimated and underestimated sea-ice areas, representing the common difference in sea-ice extent (Goessling *et al.*, 2016). The ME is the residual (i.e., IIEE minus AEE), indicative of too much ice in one place and too little in another. In the C_{oper} and C_{static} forecasts, the IIEE is generally dominated by the AEE (Figure 4), indicting that the underestimation of sea-ice loss is dominating the signal in this summer period. The only exception is the C_{oper} forecasts in the Eurasian sector (red lines in Figure 4c), where the AEE and ME are of comparable magnitudes.

3.2 | Forecasts of the atmospheric boundary layer

In this section we examine the impact of different sea-ice coupling configurations on forecasts of the atmospheric BL. To start with, we want to identify any systematic differences in the pan-Arctic atmospheric BL between the three sets of forecasts. To do this, we compute the differences

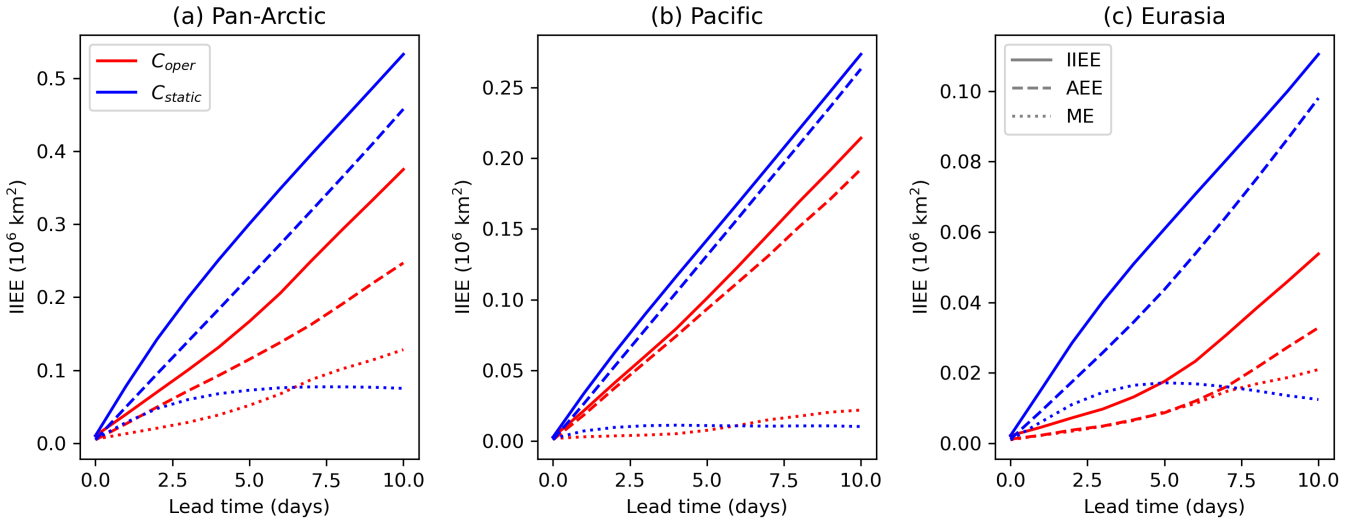

FIGURE 4 The integrated ice-edge error (IIEE) of the C_{oper} (red) and C_{static} (blue) forecasts relative to the ECMWF OCEAN5 operational analysis averaged over all forecasts as a function of lead time for the (a) Pan-Arctic, (b) Pacific, and (c) Eurasian sectors. The solid lines denote the full IIEE metric, whilst the dashed and dotted lines denote the absolute extent error (AEE) and misplacement error (ME), respectively.

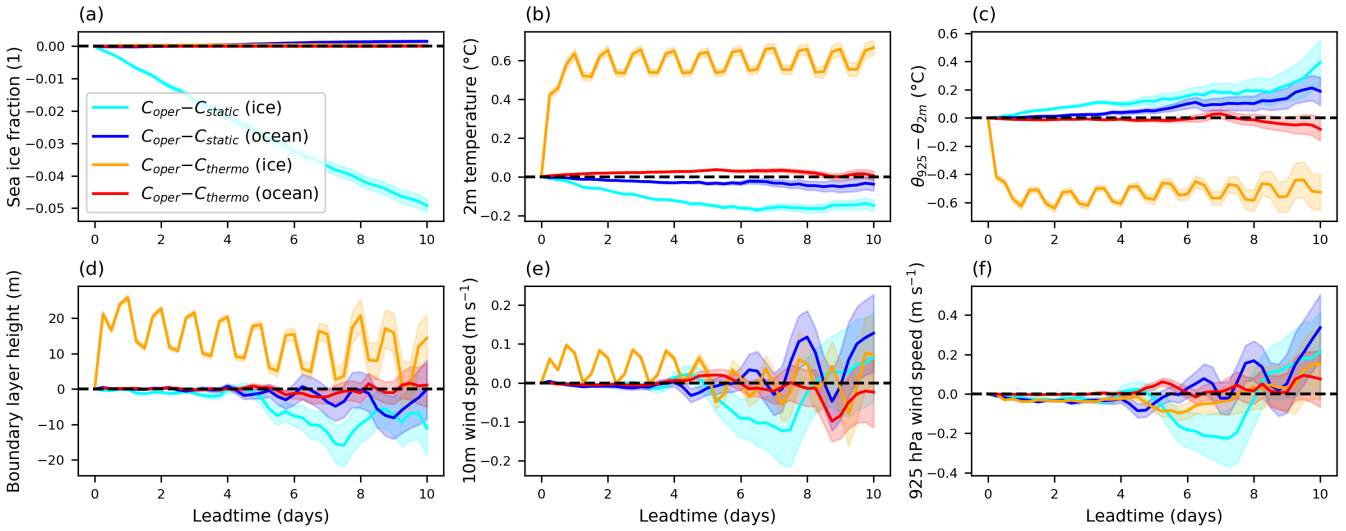

FIGURE 5 The pan-Arctic differences between forecast experiments averaged over all forecasts in (a) sea-ice fraction, (b) 2-m temperature, (c) low-level stability as diagnosed by the difference in potential temperature (θ) between 925 hPa and 2m ($\theta_{925} - \theta_{2\text{ m}}$), (d) boundary-layer height, (e) 10-m wind speed, and (f) 925-hPa wind speed, as a function of lead time. The differences are calculated as areal averages (over grid points north of 65°N that are ocean and sea ice at the forecast starts separately) for each forecast, and then averaged over all forecast start dates. The differences are presented for $C_{\text{oper}} - C_{\text{static}}$ over sea ice (cyan profiles) and ocean (blue profiles), and for $C_{\text{oper}} - C_{\text{thermo}}$ over sea ice (orange profiles) and ocean (red profiles). The solid lines denote the composite mean, and the shading denotes the standard error (calculated as the standard deviation in areal average differences divided by the square root of the number of forecasts).

in selected BL quantities averaged over all forecast start dates as a function of lead time (Figure 5). For this initial investigation, the differences are considered over grid points north of 65°N that are ocean (SIF < 0.15) and sea ice (SIF > 0.15) at the start of the forecasts, separately.

Over ice, the C_{oper} forecasts are associated with a reduction in SIF that grows with time compared with C_{static}, consistent with the analysis in Section 3.1 (Figure 5a; note that over ocean there is a slight increase in SIF in C_{oper} representing the formation of sea ice in some regions). The reduced SIF in C_{oper} is associated with systematically cooler 2-m temperatures compared with C_{static} (Figure 5b). This difference grows with time through the forecast and is larger over sea ice than ocean, approaching magnitudes

of ∼ 0.2 and ∼ 0.05°C at day 10 over ice and ocean respectively. Note that this difference is also seen in the skin temperature, with a comparable magnitude (not shown). The reduced surface and near-surface temperatures are a consequence of the melting ice in C_{oper}, with a greater fraction of exposed ocean surface (which will have a SST of −1.8 °C, the freezing point of saline water) resulting in a reduced warm bias in the grid-box average temperature. The BL over sea ice is stable in the experiments (not shown), due to the overlying atmosphere being warmer than the surface. C_{oper} is associated with even greater low-level stability than C_{static}, as indicated by a greater contrast in potential temperature (θ) from 925 hPa to 2m ($\theta_{925} - \theta_{2\text{ m}}$), particularly over ice but also over the ocean (Figure 5c). The difference in low-level stability has the same order of magnitude as the difference in 2-m temperature, suggesting that the low-level cooling due to sea-ice loss causes the increased BL stability in the C_{oper} forecasts. This is consistent with lower BL heights in C_{oper} (due to reduced turbulent mixing), although differences that are distinguishable from zero are not seen until after day 4 (Figure 5d). C_{oper} is also associated with slightly weaker winds at 10 m (Figure 5e) and 925 hPa (Figure 5f) over sea ice between days 5 and 8. The BL height-difference profiles in Figure 5d follow similar patterns to those of the low-level wind in Figure 5e,f, suggesting that the BL turbulence is wind-driven. Although weaker winds are consistent with a more stable BL in C_{oper}, the differences are of very low magnitude (of the order of 0.1 m s^{-1}), with a relatively large standard error. This indicates that there is not a systematic difference in wind speed between the two experiments.

The SIF in C_{oper} is virtually identical to that in C_{thermo}, with the orange and red lines being indistinguishable from zero at all lead times in Figure 5a. However, C_{thermo} exhibits 2-m temperatures over ice that are ∼ 0.6°C cooler than in C_{oper} (Figure 5b), consistent with greater low-level stability (Figure 5c). This suggests reduced BL turbulent mixing in C_{thermo}, which is consistent with lower BL heights (Figure 5d) and weaker 10-m winds (Figure 5e, at least in the first five days of the forecasts). The difference in 2-m temperature exhibits a diurnal cycle, which also feeds into low-level stability, BL height, and 10-m wind. This occurs due to there being a larger diurnal variation in C_{oper} (where temperatures can exceed zero over ice) than in C_{thermo}. The reduction in low-level temperatures of ∼ 0.6°C is similar in magnitude to the warm bias in Tjernström *et al.* (2021), indicating that the surface temperature and albedo coupling eliminates the warm bias. The C_{thermo} near-surface temperatures are the same as the other experiments at the initial time (with the same warm bias over ice), and then cool rapidly at the first coupling step, explaining the sharp change between days 0 and 1 in Figure 5b (this is the "initialisation shock" described in Section 2.1). Again, the same differences are seen in the skin temperature, with the same magnitude (not shown). The cooler temperatures in C_{thermo} largely remain local to the sea ice, with only small differences over the ocean (Figure 5b). The differences in 925-hPa wind between C_{oper} and C_{thermo} are rather small with large standard errors (Figure 5f), indicating that there is no systematic difference.

The differences in Figure 5 are small, due to taking pan-Arctic averages over all forecasts. To understand the impact of the sea-ice coupling better, we must examine selected forecasts in more detail in time and space. To maximize the potential signal, here we will examine forecast start dates where the surfaces in C_{oper} and C_{static} are most different, as presumably this will prompt the greatest impact on the overlying atmosphere. Forecasts will be compared in the previously defined Pacific and Eurasian sectors separately, providing two case periods with different sea-ice conditions and meteorology (see Sections 3.2.1 and 3.2.2). Note that we will use the same dates for comparison of the C_{thermo} forecasts for continuity. The focus hereafter is on three-day forecasts, as at longer lead times the atmospheric forecasts were found to have diverged significantly in some cases due to the chaotic nature of the system, making direct attribution to model differences more difficult.

The differences in SIF between C_{oper} and C_{static} over three-day forecasts in the Pacific and Eurasian sectors are presented in Figure 6. In both regions, the greatest SIF difference between the two experiments at three days is found to occur over four consecutive forecasts (exceeding the 90th percentile of difference), and these are chosen as case periods for further study. In the Pacific, the greatest difference in SIF between the forecasts occurs in late July, in association with cyclone "2" (Figure 6a). Note that this is the aforementioned cyclone that was studied in Croad *et al.* (2023a). The "Pacific case period" for further examination is comprised of three-day forecasts starting on July 26–29. In the Eurasian sector, the greatest difference in SIF between the forecasts occurs in mid-August, associated with cyclones "7" and "8" (Figure 6b). The "Eurasian case period" is comprised of three-day forecasts starting on August 13–16.

3.2.1 | Pacific case period: Forecasts starting July 26–29

Composite maps describing the surface in the Pacific sector from three-day forecasts starting on July 26–29 are presented in Figure 7. In this region the MIZ spans a broad meridional extent in C_{oper} from 70–80°N, with the SIF being largely between 0.5 and 0.8, with a very sharp

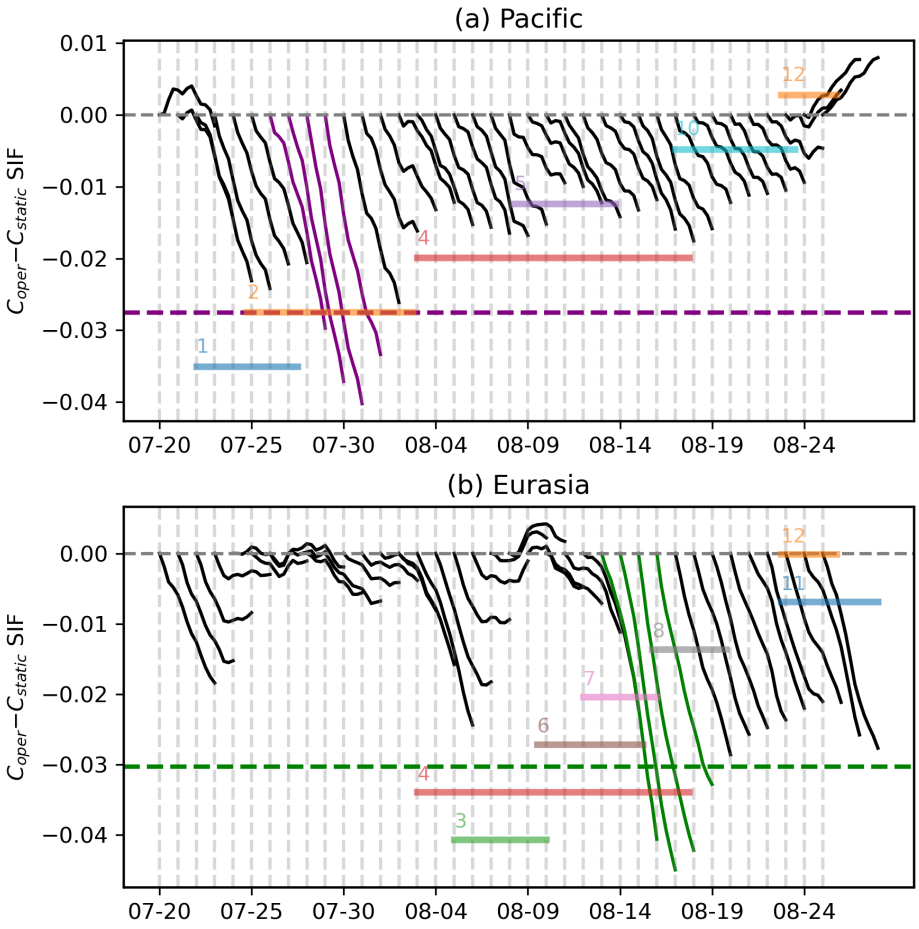

FIGURE 6 Time series of the areal average difference in SIF ($C_{oper} - C_{static}$) over three-day forecasts in the (a) Pacific and (b) Eurasian sectors. The dashed horizontal lines mark the 90th percentile of three-day differences for each region, and the solid lines coloured in purple and green denote the forecast start dates that exceed this threshold in the (a) Pacific and (b) Eurasian sectors respectively. The semi-transparent horizontal lines refer to the passage of cyclones, with the colours and numbers matching those in Figure 2c.

drop-off to 0.15 approaching the ice edge (Figure 7a). Cyclone 2 is seen in the mean sea-level pressure (MSLP) field, positioned directly over the MIZ during this time, with the cyclone centre over a small gap in the ice (where the SIF has fallen below 0.5). Beneath the cyclone, C_{oper} is associated with reduced SIF compared with C_{static} (Figure 7b), suggesting that cyclone 2 is associated with the breakup and melting of ice in the coupled forecasts. C_{oper} has greater SIF along the ice edge to the west of the Pacific sector, which is likely associated with the advection of ice by large-scale off-ice flow associated with the cyclone. C_{thermo} is associated with slightly higher SIF than C_{oper} (perhaps due to the colder surface and near-surface temperatures identified in Figure 5 inhibiting melting), but the differences are approximately an order of magnitude smaller than the differences between C_{oper} and C_{static} (Figure 7c). C_{oper} and C_{thermo} have an areal average SIF in the Pacific sector (i.e., the purple box) that is almost identical to the EPS ensemble mean, whereas C_{static} has a higher areal average SIF than any of the ensemble members (Figure 7d).

The MIZ region is associated with relatively large surface roughness lengths compared with the surrounding ocean and pack ice (Figure 7e). This is because, in the IFS Cy47r1, the roughness length for momentum depends on SIF and peaks when SIF is approximately 0.5 (ECMWF, 2020). C_{oper} has reduced SIF compared with C_{static} (Figure 7b), and, given that the SIF is largely between 0.5 and 0.8 (Figure 7a), this means that the SIF in C_{oper} is moving closer to 0.5 with greater surface roughness lengths than C_{static} (Figure 7f). This is generally true except in the small gap of ice in C_{oper}, where the SIF moves away from 0.5. In this region, C_{oper} has reduced roughness lengths compared with C_{static}, as the SIF falls below 0.5. The slightly greater SIF in C_{thermo} than C_{oper} means that the surface roughness lengths are reduced in C_{thermo}, but the differences are an order of magnitude smaller than those between C_{oper} and C_{static} (Figure 7g).

Maps of the differences in BL quantities from the three sets of forecasts are presented in Figure 8. As seen from Figure 5b, the near-surface temperatures are reduced in C_{oper} compared with C_{static} over almost the entire domain (Figure 8a). The magnitude of this cooling is greatest where the SIF has been reduced in C_{oper} compared with C_{static}, with a value of ~ 0.5°C in the gap in the sea ice in the middle of the domain. Differences in surface sensible and latent heat fluxes between the experiments are found to have the same sign and have similar magnitudes,

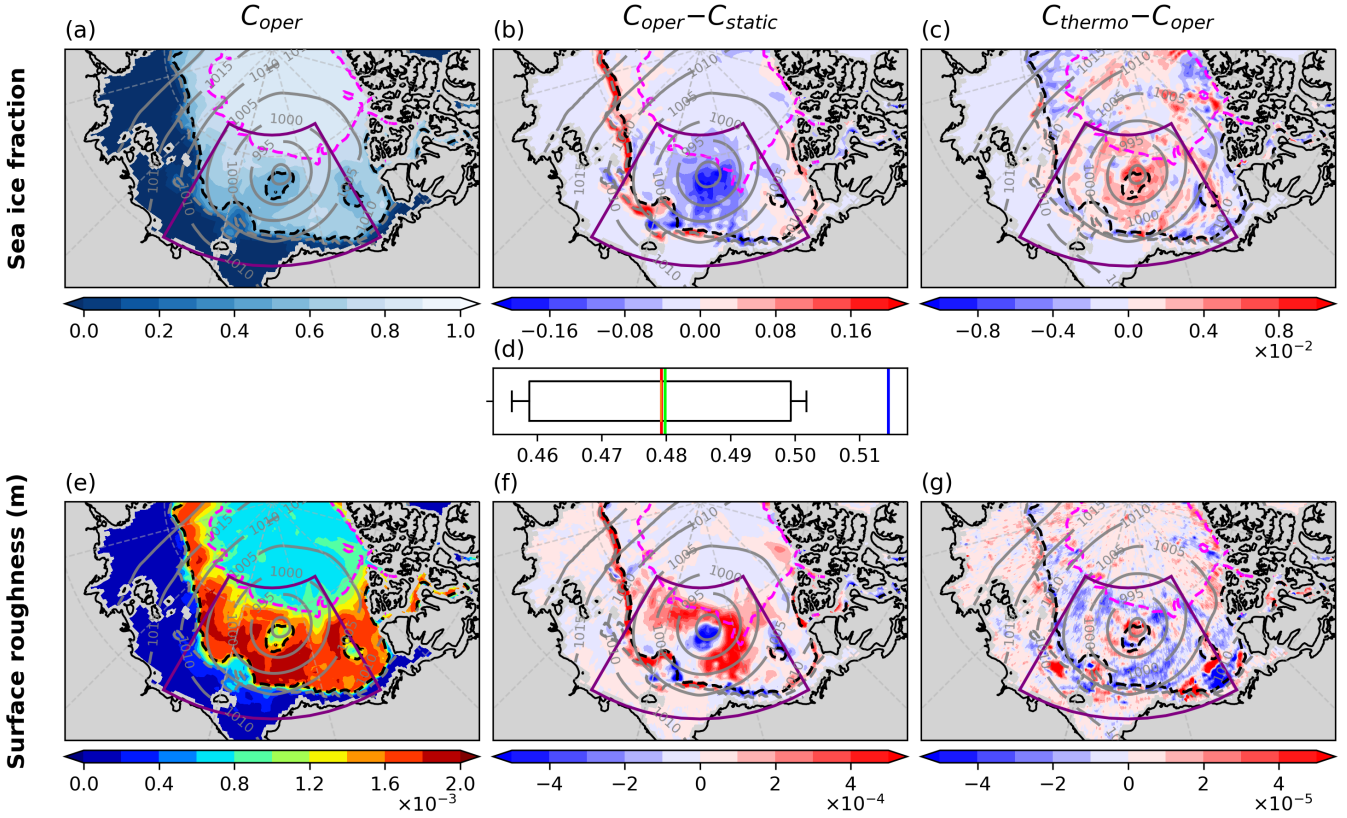

FIGURE 7 Composite mean SIF and surface roughness lengths for three-day forecasts starting on July 26–29, 2020. The top panels are maps of (a) average SIF in C_{oper}, (b) the average difference in SIF between C_{oper} and C_{static}, and (c) the average difference in SIF between C_{thermo} and C_{oper}. (d) The average SIF in the purple region from C_{oper} (red line), C_{static} (blue line), C_{thermo} (lime green line), and each EPS ensemble member presented as a box plot (with whiskers extending to the maximum and minimum values). The bottom panels (e–g) are as (a–c) but for surface roughness length. Note the differences in order of magnitude when comparing panels (b) and (c), and (f) and (g). Contours of SIF (0.15, grey dashed; 0.5, black dashed; 0.8, magenta dashed) and mean sea-level pressure (grey solid) from (a,e) C_{oper}, (b,f) C_{static}, (c,g) C_{thermo} are overlaid.

so are combined into one field for this analysis. The lower near-surface temperatures over the centre of the domain are associated with surface sensible and latent heat fluxes that are more negative in C_{oper} than in C_{static} (Figure 7b), indicating greater heat and moisture transfer from the atmosphere to the surface. This is consistent with a more stable BL over ice in C_{oper}. There is also a notable reduction in near-surface temperature in the off-ice flow to the west of the Pacific sector in the Laptev Sea (Figure 8a). This results in more positive sensible and latent heat fluxes in C_{oper} than in C_{static} (Figure 8b), with more heat and moisture transfer from the surface to the atmosphere due to a greater temperature contrast between the ocean surface and the air. In this case over the ocean, the BL is more unstable in C_{oper}. Furthermore, the 10-m wind speeds in the cyclone are found to be ~0.5 m s^{-1} lower in C_{oper} than in C_{static} (Figure 8c). The weaker winds are associated with greater surface momentum fluxes over the MIZ on the eastern flank of the cyclone (Figure 8d). This indicates that the weaker winds in C_{oper} are linked to increased surface roughness and surface drag in the MIZ.

The C_{thermo} forecasts have near-surface temperatures that are up to 1.0 °C cooler over ice compared with C_{oper} (Figure 8e). This large difference in near-surface temperature is associated with sensible and latent heat fluxes that are more negative over all ice in C_{thermo} (Figure 8f), meaning greater heat and moisture transfer from the atmosphere to the surface, consistent with a more stable BL. Also note that there are slightly colder temperatures over the ocean in C_{thermo} (Figure 8e), associated with more positive sensible and latent heat fluxes (Figure 8f). This indicates greater heat and moisture transfer from the ocean surface to the overlying atmosphere, in the opposite sense to the fluxes over ice. C_{thermo} is consistently associated with slightly weaker winds than C_{oper} over the ice (Figure 8g), but also reduced surface momentum flux (Figure 8h). This indicates that the weaker winds in C_{thermo} are related to increased BL stability over ice.

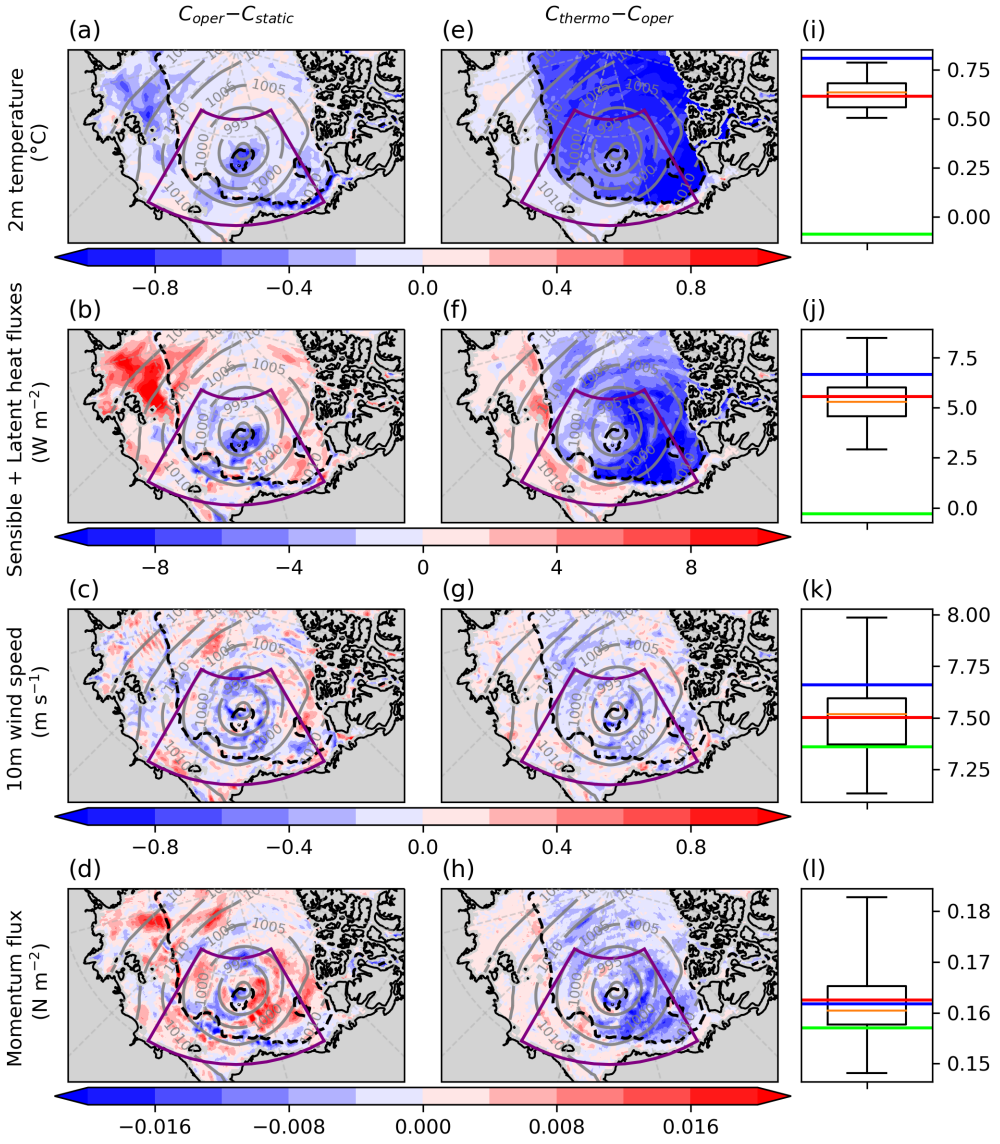

FIGURE 8 Composite mean differences in BL quantities for three-day forecasts starting on July 26–29, 2020. The top row shows the 2-m temperature, with (a) the average difference between C_{oper} and C_{static}, (e) the average difference between C_{thermo} and C_{oper}, and (i) the areal average value over sea-ice grid points at the forecast starts in the purple region from C_{oper} (red line), C_{static} (blue line), C_{thermo} (lime green line), and each EPS ensemble member presented as a box plot (with whiskers extending to the maximum and minimum values). Panels (b, f, j), (c, g, k), and (d, h, l) are as (a, e, i) but for the sum of surface sensible and latent heat fluxes, 10-m wind speed, and momentum flux, respectively. Contours of 0.5 SIF (black dashed) and mean sea-level pressure (grey solid) from C_{oper} are overlaid on each map.

This analysis demonstrates differences in BL quantities between the forecast experiments that are physically consistent with the changes at the surface. The differences in near-surface temperature between the experiments are relatively large compared with the spread of the EPS ensemble, with C_{static} being slightly warmer than any other ensemble member, C_{oper} aligning with the ensemble mean, and C_{thermo} being much cooler than any other ensemble member (Figure 8i). Note that the average 2-m temperature over ice has been reduced from ~0.6 °C in C_{oper} to just below 0 °C in C_{thermo}, demonstrating that the C_{thermo} configuration has corrected for the known warm bias over ice. The difference in the sum of the surface sensible and latent heat fluxes between C_{oper} and C_{static} has a regional dependence (Figure 8b), and so the average difference is small compared with the spread of the EPS ensemble (Figure 8j). In contrast, the systematically more negative sensible and latent heat fluxes over ice in C_{thermo} than in C_{oper} (Figure 8f), with an average value of approximately 0 W m^{-2} compared with ~5 W m^{-2}, is a relatively large difference compared with the spread of the EPS ensemble (Figure 8j). The differences in 10-m wind (Figure 8k) and surface momentum flux (Figure 8l) between the three sets of experiments are small compared with the spread of the EPS ensemble.

3.2.2 | Eurasian case period: Forecasts starting August 13–16

Figure 9 shows composite maps describing the surface in the Eurasian sector from three-day forecasts starting on August 13–16. The sea-ice field differs from that during the Pacific case period, with a sharp drop in SIF from pack ice to open ocean, constituting a very narrow MIZ (Figure 9a). The MSLP field highlights a cyclone to the southeast of

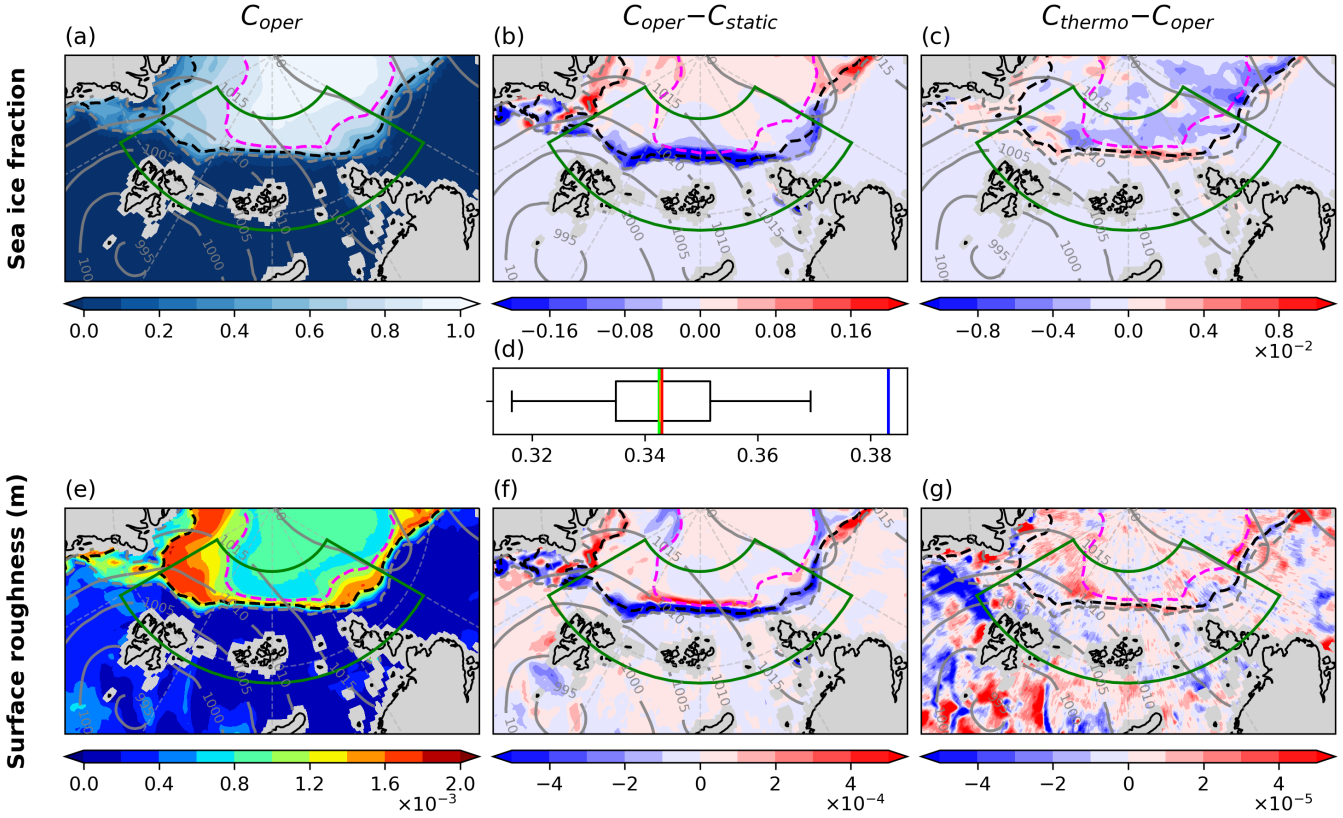

FIGURE 9 As in Figure 7 but for three-day forecasts starting on August 13–16, 2020 in the Eurasian sector. Note the differences in order of magnitude when comparing panels (b) and (c), and (f) and (g).

Svalbard, resulting in on-ice flow in the Eurasian sector (Figure 9a; note that cyclones 7 and 8 merge into one system south of Svalbard, see tracks in Figure 2c). The cyclonic flow is likely responsible for transporting heat poleward, resulting in the reduction of SIF in a narrow band at the ice edge in C_{oper} compared with C_{static} (Figure 9b). There is also a complicated change in ice-edge geometry in the off-ice flow to the west of the domain, with increased SIF to the north of Greenland (likely related to transport of ice by the wind forcing) and reduced SIF to the east of Greenland (perhaps usual summer melting) in C_{oper} compared with C_{static}. The differences in SIF between C_{thermo} and C_{oper} are again an order of magnitude smaller than that between C_{oper} and C_{static} (Figure 9c). The areal average SIF in the green box from C_{oper} and C_{thermo} is almost identical to the EPS ensemble mean, whereas C_{static} has a higher areal average SIF than any other ensemble member (Figure 9d).

The surface roughness over ice is generally lower than during the Pacific case period, due to the narrower MIZ region (Figure 9e). The reduction in SIF at the ice edge in C_{oper} (Figure 9b) is associated with a dipole in the difference in surface roughness lengths compared with C_{static}, with lower surface roughness where the SIF falls below 0.5 at the outermost edge and greater surface roughness behind where SIF falls closer to 0.5 (Figure 9f). The differences in surface roughness between C_{oper} and C_{thermo} are again small (Figure 9g).

C_{oper} is associated with reduced 2-m temperatures compared with C_{static} where ice loss has occurred, on the ice edge and in the off-ice flow to the west of the domain (Figure 10a). The reduced near-surface temperatures are again associated with more negative surface sensible and latent heat fluxes in C_{oper} than C_{static} (Figure 10b), indicating a more stable BL in C_{oper} in these regions. C_{oper} is associated with a thin band of enhanced 10-m wind speeds on the ice edge compared with C_{static} (Figure 10c), where SIF has been reduced below 0.5 and therefore the surface is less rough (Figure 9b,f), with reduced surface momentum fluxes (Figure 10d). This demonstrates that the reduced surface roughness over ice in C_{oper} compared with C_{static} results in a local increase in 10-m wind speed due to reduced surface drag. The 10-m wind speed is also enhanced in C_{oper} in the off-ice flow to the west of the domain (Figure 10c), which may be associated with the reduced surface roughness in this region (Figure 9f).

As in the Pacific case period, C_{thermo} is associated with reduced near-surface temperatures over ice compared with C_{oper} (Figure 10e), with a difference of ~ 0.5°C. These cooler temperatures are associated with sensible

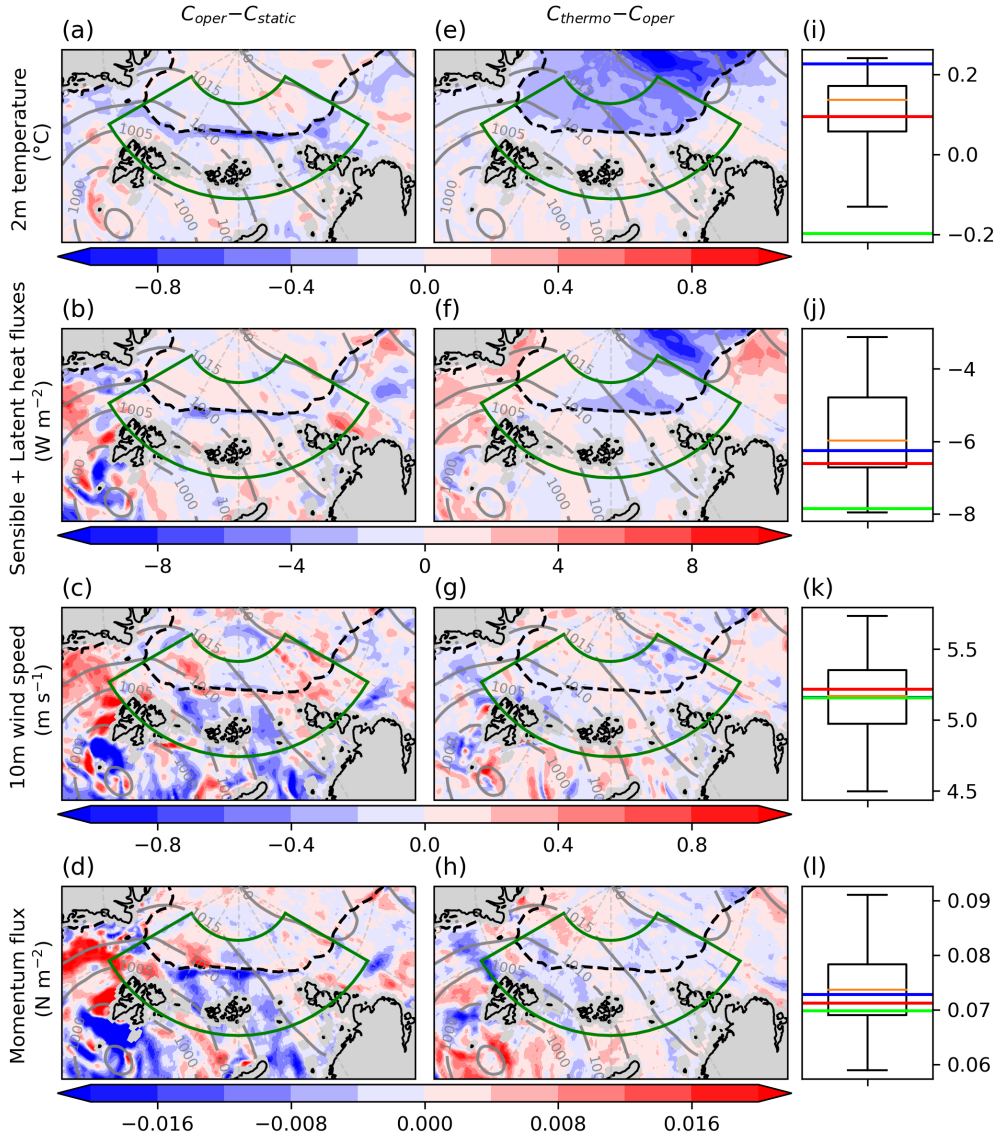

FIGURE 10 As in Figure 8, but for three-day forecasts starting on August 13–16, 2020 in the Eurasian sector.

and latent heat fluxes that are more negative over ice in the on-ice flow, but more positive over ocean in the off-ice flow (Figure 10f) in C_{thermo}, as was seen in the Pacific case period (Figure 8f). The on-ice flow in C_{thermo} (where BL stability is greater) is associated with slightly weaker 10-m winds (Figure 10g) and reduced surface momentum fluxes (Figure 10h) compared with C_{oper}, but the differences are generally small.

Again, the differences in BL quantities are physically consistent with the changes at the surface. The differences in the 2-m temperature are again relatively large compared with the spread of the EPS ensemble (Figure 10i), but the differences in surface sensible and latent heat fluxes, 10-m wind, and surface momentum fluxes (Figure 10j–l) are relatively small compared with the EPS ensemble and the Pacific case period. Note again that the C_{thermo} configurations correct the known warm bias over ice, with the average 2-m temperatures being below zero, in contrast to the C_{oper} and C_{static} configuations (Figure 10i). The differences are generally smaller in this case, due to the domain of interest containing less sea ice and any differences in the sea-ice surface between C_{oper} and C_{static} occupying a smaller areal extent (compared with the Pacific case period). This analysis demonstrates that the impact of sea-ice coupling largely remains local to the sea ice itself, and that the size of the impact is dependent on the areal extent of the ice (when comparing C_{oper} and C_{thermo}) and the areal extent of the sea-ice changes (when comparing C_{oper} and C_{static}).

3.3 | Forecasts of Arctic cyclones

The MSLP fields in Figures 7 and 9 indicate that the differences between the cyclones in the three sets of forecasts are small, but in this section we examine the impact of

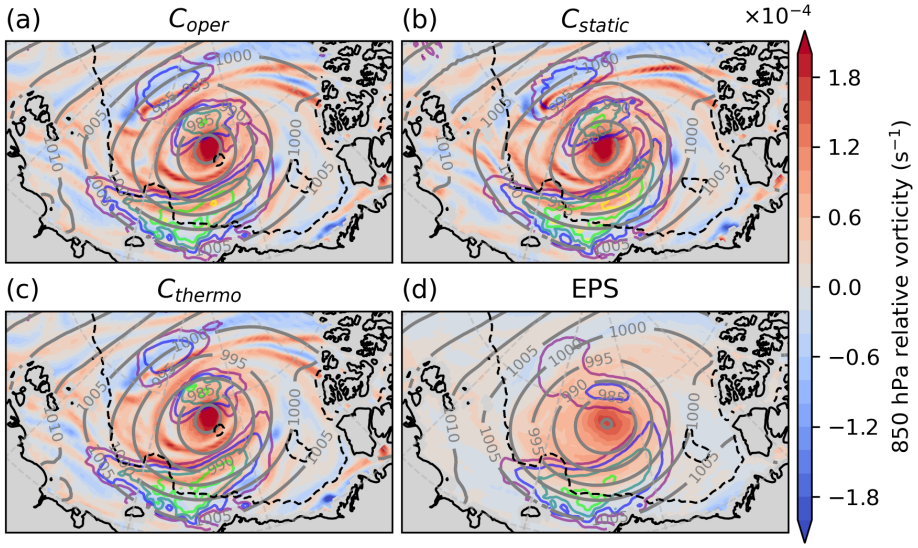

FIGURE 11 Maps of cyclone 2 from three-day forecasts starting on July 26 (valid July 29). The maps display 850-hPa relative vorticity (shading), 10-m wind speed speeds (solid coloured contours from 10–15 m s^{-1}), mean sea-level pressure (grey contours), and 0.5 SIF fraction (black dashed contours) from (a) C_{oper}, (b) C_{static}, (c) C_{thermo}, and (d) the EPS ensemble mean.

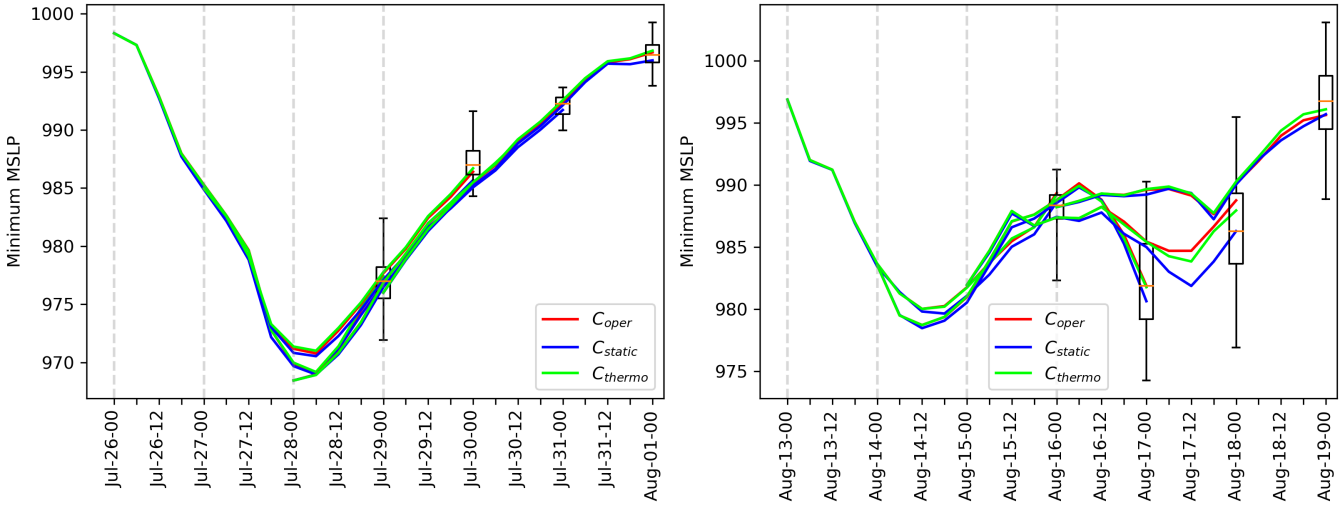

FIGURE 12 The minimum mean sea-level pressure from three-day forecasts for (a) cyclone 2 during the Pacific case period with forecast start dates July 26–29, and (b) cyclones 7 and 8 (combined into a single cyclone track) during the Eurasian case period with forecast start dates August 13–16, from C_{oper} (red), C_{static} (blue), and C_{thermo} (lime green). The EPS ensemble at day 3 is presented by the box plots (with whiskers extending to the maximum and minimum values).

sea-ice coupling on Arctic cyclones in more detail. Firstly, maps of cyclone 2 from three-day forecasts starting on July 26 (valid July 29) are presented in Figure 11. The forecasts of 850-hPa relative vorticity are remarkably similar from C_{oper}, C_{static}, and C_{thermo} (Figure 11a–c), with large positive values at the centre of the cyclone and banded features further from the centre. There are some small discernible differences in the 10-m wind speed to the south of the cyclone, with C_{static} having slightly stronger winds over a larger area than C_{oper}, which has slightly stronger winds than C_{thermo} (seen by focusing on the 15 m s^{-1} contours in Figure 11a–c). These differences in wind speed at 10 m are consistent with the analysis in Section 3.2. The EPS ensemble mean map is much smoother in 850-hPa relative vorticity than the individual forecast experiments (Figure 11d), indicating variability in cyclone placement amongst the ensemble members. This suggests that the differences between the EPS ensemble members are larger than those between the C_{oper}, C_{static}, and C_{thermo} forecasts.

Time series of cyclone intensity, as diagnosed by minimum MSLP, from three-day forecasts are presented in Figure 12. The minimum MSLP in each forecast is found by searching for the minimum value within a 500-km radius of the ERA5 cyclone centre determined by TRACK (see Section 2.3). Forecasts of strength for cyclone 2 during the Pacific case period (Figure 12a) are remarkably similar across different forecast experiments and forecast start times. C_{static} consistently has the lowest minimum MSLP

and C_{thermo} consistently has the highest; however, the differences at three days are of the order of only 1 hPa. The differences in cyclone strength at three days are smaller than the spread of the EPS ensemble, shown by the box plots in Figure 12a. Forecasts of strength for cyclones 7 and 8 (combined into one track here) during the Eurasian case period (Figure 12b) exhibit larger differences between the forecast experiments and forecast start times, indicative of a more uncertain situation due to the merger of the two systems. This is reflected by the larger spread of the EPS ensemble in Figure 12b. Again, the differences in cyclone strength at three days are smaller than the spread of the EPS ensemble.

This analysis demonstrates that the impact of the sea-ice coupling on the forecasts of Arctic cyclones is smaller than the impact of the noise of the initial condition and stochastic perturbations to the ensemble members in the prediction system. From Section 3.2, changing the sea-ice coupling can have locally large impacts on the near-surface temperature (up to 1 °C) and near-surface winds (up to 0.5 m s^{-1}) in the BL, but these impacts are generally isolated to the sea ice (when comparing C_{oper} and C_{thermo}), or to regions where sea-ice change has occurred (when comparing C_{oper} and C_{static}). Hence, the overall impact of the sea-ice coupling on the larger scales above the BL is very small. Cyclone 2 during the Pacific case period represents a set-up that should maximise the differences between the three sets of forecast experiments, with the cyclone being positioned over the MIZ for several days (Figure 7). However, the cyclone has a similar position and strength in each forecast experiment (Figures 11 and 12a). The analysis here and in Section 3.2 has focused on three-day forecasts. Similar results were found with six-day forecasts, although the impact of the sea coupling had a weaker signal, with the forecasts diverging due to chaos (not shown).

4 | CONCLUSIONS

With climate change, sea ice is becoming thinner and more mobile in the summer-time Arctic, making it more susceptible to breakup and melting by atmospheric forcings such as cyclones. Hence, static sea ice for weather forecasts is an increasingly poor assumption in the summer-time Arctic. In recent years, the ECMWF has implemented ocean–ice–atmosphere coupling with dynamic sea ice in the IFS at all time ranges. Day *et al.* (2022) demonstrated that dynamic sea ice in the IFS generally improved medium-range forecasts in the Arctic in a winter case study. However, no corresponding evaluation for summer has been published in the literature. Despite recent advances, the IFS has a known warm bias over sea ice in summer (Tjernström *et al.*, 2021), which may be related to the fact that the sea ice is not coupled thermodynamically.

In this study we examine the sensitivity of IFS weather forecasts to sea-ice coupling in the summer-time Arctic, by comparing three sets of 10-day forecast experiments from IFS Cy47r1 that differ only in their sea-ice coupling configurations. The results are based on the period July 20–August 25, 2020, although we expect that the qualitative conclusions could be extended to the broader Arctic summer period, in a melting regime. The first set of forecasts, C_{oper}, is identical to the control member of the operational EPS ensemble used at the time, with "dynamic sea ice". The second set of forecasts, C_{static}, is identical to C_{oper} except that it has "static sea ice", where the sea-ice field cannot evolve from the start of the forecast as was operational in the EPS prior to November 2016. The third set of forecasts, C_{thermo}, is an experimental setup that is identical to C_{oper}, except with additional "thermodynamic coupling" (sea-ice surface temperature and albedo coupled to the atmosphere as well as SIF).

The first research question was to understand where the dynamic coupling with the ocean–sea-ice model has the greatest impact on sea-ice forecasts (Section 3.1). It was found that dynamic sea ice had the greatest impact in the vicinity of Arctic cyclones. The dynamic sea-ice forecasts capture cyclone-induced breakup and melting of sea ice due to strong winds and warm-air intrusions, whereas the static sea-ice forecasts cannot. However, ice loss was underestimated in the dynamic sea-ice forecasts, which may be attributed to missing ocean wave processes or model biases in sea-ice thickness. Despite this, the dynamic sea-ice forecasts produced much improved sea-ice field and ice-edge predictions compared with the static sea-ice forecasts.

The second and third research questions were to understand the impact of dynamic sea ice and additional thermodynamic coupling on forecasts of the atmospheric BL (Section 3.2). The forecasts with dynamic sea ice were found to have colder near-surface temperatures than the static sea-ice forecasts (up to ~ 0.5°C in regions where sea-ice cover is reduced), with consistent changes in surface heat fluxes and BL stability. Differences in surface momentum fluxes and low-level winds were found to depend on changes to the surface roughness of the sea ice when comparing the dynamic and static sea-ice forecasts. For example, an extreme cyclone in late July (cyclone 2) was positioned over the MIZ for several days, with rougher sea ice in the dynamic sea-ice forecasts resulting in a reduction in 10-m winds of ~0.5 m s^{-1} over a broad area. The forecasts with additional thermodynamic coupling had near-surface temperatures over sea ice that were up to ~ 1.0°C cooler than the operational forecasts, correcting

the known warm bias over ice. This was found to be consistent with a more stable BL and weaker 10-m winds over sea ice of up to ~0.5 m s^{-1}.

While the sea-ice coupling was found to have locally large impacts on near-surface temperature and winds, the impacts were generally limited to near the sea-ice surface. The size of impact was dependent on the areal extent of sea ice and sea-ice changes. For example, larger differences were found in a Pacific case period where a cyclone was positioned over the MIZ for several days than in a Eurasian case period where the cyclone centre was located south of the ice edge. In general, other than near-surface temperature, the differences between the three experiments were found to be smaller than the spread of the EPS ensemble.

The final research question was to understand if sea-ice coupling impacted forecasts of Arctic cyclones (Section 3.3). Examining two case periods, it was determined that the differences between the cyclones in the three forecasts were smaller than the spread of the operational ensemble. This suggests that any impact of sea-ice coupling on the larger scales above the BL is very small in the model, compared with the growth of forecast uncertainty from initial conditions and model physics.

In summary, this work demonstrates the benefits of increasingly sophisticated sea-ice coupling representations in a NWP model in the summer-time Arctic, with physically consistent impacts on forecasts. This work has also highlighted the limitations of the sea-ice coupling used operationally in the IFS, with the simplistic SIF coupling not capturing any ocean wave interactions and not correcting for a surface energy imbalance that leads to a low-level warm bias. The latter was addressed by implementing an experimental configuration with additional thermodynamic coupling. The impact of closer thermodynamic coupling (including the representation of snow on ice), and how this can be employed with adaption to the current data assimilation systems, is being assessed across all ECMWF forecast systems for future implementation, as part of continuously ongoing efforts to improve Earth-system interactions in the IFS. This study, along with observation-based evaluations of surface exchange parametrisations over ice (e.g., Elvidge *et al.*, 2016, 2021, 2023; Srivastava *et al.*, 2022), highlights the need to revisit how surface exchange is modelled in the coupled system.

With regards to cyclone–sea-ice interaction in the model, the results of this work suggest that cyclones have a larger impact on sea ice than sea ice does on cyclones during summer. Whether this result is model-specific (e.g., due to the underestimation of ice loss with missing processes in the model) or whether it is relevant to the physical world should be determined. The emphasis for future work should be placed on evaluation of the NWP model output in the Arctic, key to which is real-world observations. In particular, the forecast experiments should be re-run for previous summer-time Arctic field campaign periods. For example, evaluation against the observations discussed in Tjernström *et al.* (2019) would permit an examination of whether the increasingly sophisticated sea-ice coupling representations result in improved model performance in the case of warm-air advection events and surface-based inversions in summer.

ACKNOWLEDGEMENTS

H. L. Croad acknowledges PhD studentship funding from SCENARIO NERC Doctoral Training Partnership grant NE/S007261/1, with co-supervision by S. P. E. Keeley and supercomputing support from ECMWF. J. Methven, B. Harvey, and A. Volonté were funded by the NERC standard grant (Arctic Summer-time Cyclones: Dynamics and Sea-Ice Interaction) grant NE/T006773/1. B. Harvey was also supported by the National Centre for Atmospheric Science, which is funded by NERC under contract R8/H12/83. The authors thank Kevin Hodges for providing cyclone tracks from the TRACK algorithm for use in this study. The authors also acknowledge the ECWMF for the production of the ERA5 reanalysis dataset.

DATA AVAILABILITY STATEMENT

ECMWF IFS forecast data were produced by running ECMWF's IFS model (model cycle 47r1, which was operational from June 30, 2020–May 10, 2021). These data are stored on ECMWF's Meteorological Archive Retrieval System (MARS) Catalogue, under experiment IDs "b2k2", "b2l7", and "b2mv". These data are not publicly available but can be provided on request. ECMWF ERA5 reanalysis data (Hersbach *et al.*, 2020) and operational forecasts from the ECMWF ensemble prediction system were also retrieved via MARS. The ERA5 reanalysis data are publicly available and can be downloaded from the Copernicus Climate Change Service (C3S) Climate Data Store (Hersbach *et al.*, 2017). The TRACK algorithm (Hodges, 1994, 1995) is available on the University of Reading's Git repository (Gitlab) at https://gitlab.act.reading.ac.uk/track/track (Hodges, 2021).

ORCID

Hannah L. Croad https://orcid.org/0000-0002-5124-4860
Sarah P. E. Keeley https://orcid.org/0000-0002-8046-765X
John Methven https://orcid.org/0000-0002-7636-6872
Ben Harvey https://orcid.org/0000-0002-6510-8181
Ambrogio Volonté https://orcid.org/0000-0003-0278-952X

REFERENCES

Arduini, G., Keeley, S., Day, J.J., Sandu, I., Zampieri, L. & Balsamo, G. (2022) On the importance of representing snow over sea-ice for simulating the Arctic boundary layer. *Journal of Advances in Modeling Earth Systems*, 14, e2021MS002777.

Asplin, M.G., Galley, R., Barber, D.G. & Prinsenberg, S. (2012) Fracture of summer perennial sea ice by ocean swell as a result of Arctic storms. *Journal of Geophysical Research – Atmospheres*, 117, C06025.

Balan-Sarojini, B., Tietsche, S., Mayer, M., Balmaseda, M., Zuo, H., De Rosnay, P. et al. (2021) Year-round impact of winter sea ice thickness observations on seasonal forecasts. *The Cryosphere*, 15, 325–344.

Balmaseda, M.A., Ferranti, L., Molteni, F. & Palmer, T.N. (2010) Impact of 2007 and 2008 Arctic ice anomalies on the atmospheric circulation: implications for long-range predictions. *Quarterly Journal of the Royal Meteorological Society*, 136, 1655–1664.

Barton, N., Metzger, E.J., Reynolds, C.A., Ruston, B., Rowley, C., Smedstad, O.M. et al. (2021) The navy's earth system prediction capability: a new global coupled atmosphere-ocean-sea ice prediction system designed for daily to subseasonal forecasting. *Earth and Space Science*, 8, e2020EA001199.

Bushuk, M., Msadek, R., Winton, M., Vecchi, G., Yang, X., Rosati, A. et al. (2019) Regional Arctic sea–ice prediction: potential versus operational seasonal forecast skill. *Climate Dynamics*, 52, 2721–2743.

Croad, H.L., Methven, J., Harvey, B., Keeley, S.P.E. & Volonté, A. (2023a) The role of boundary layer processes in summer-time Arctic cyclones. *Weather and Climate Dynamics*, 4, 617–638.

Croad, H.L., Methven, J., Harvey, B., Keeley, S.P.E., Volonté, A. & Hodges, K.I. (2023b) A climatology of summer-time Arctic cyclones using a modified phase space. *Geophysical Research Letters*, 50, e2023GL105993.

Day, J.J., Keeley, S., Arduini, G., Magnusson, L., Mogensen, K., Rodwell, M. et al. (2022) Benefits and challenges of dynamic sea ice for weather forecasts. *Weather and Climate Dynamics*, 3, 713–731.

Donlon, C.J., Martin, M., Stark, J., Roberts-Jones, J., Fiedler, E. & Wimmer, W. (2012) The operational sea surface temperature and sea ice analysis (OSTIA) system. *Remote Sensing of Environment*, 116, 140–158.

Ebert, E.E. & Curry, J.A. (1993) An intermediate one-dimensional thermodynamic sea ice model for investigating ice-atmosphere interactions. *Journal of Geophysical Research, Oceans*, 98, 10085–10109.

ECMWF (2020) *IFS documentation Cy47r1, Part IV: Physical Processes*. https://www.ecmwf.int/en/elibrary/81189-ifs-documentation-cy47r1-part-iv-physical-processes.

ECMWF (2023a) Forecast user guide: Section 2.1.4.8 water-surface temperature and ice concentration. https://confluence.ecmwf.int/display/FUG/Section+2.1.4.8+Water-surface+temperature+and+ice+concentration

ECMWF (2023b) Forecast user guide: Section 2.2 ocean wave model - ecwam. https://confluence.ecmwf.int/display/FUG/Section+2.2+Ocean+Wave+Model+-+ECWAMSection2.2OceanWaveModelECWAM-Nearseaice

ECMWF (2024) Forecast user guide: Section 2.1.4.3 modelling ocean surfaces. https://confluence.ecmwf.int/display/FUG/Section+2.1.4.3+Modelling+ocean+surfaces

Elvidge, A., Renfrew, I., Weiss, A., Brooks, I., Lachlan-Cope, T. & King, J. (2016) Observations of surface momentum exchange over the marginal ice zone and recommendations for its parametrisation. *Atmospheric Chemistry and Physics*, 16, 1545–1563.

Elvidge, A.D., Renfrew, I.A., Brooks, I.M., Srivastava, P., Yelland, M.J. & Prytherch, J. (2021) Surface heat and moisture exchange in the marginal ice zone: observations and a new parameterization scheme for weather and climate models. *Journal of Geophysical Research – Atmospheres*, 126, e2021JD034827.

Elvidge, A.D., Renfrew, I.A., Edwards, J.M., Brooks, I.M., Srivastava, P. & Weiss, A.I. (2023) Improved simulation of the polar atmospheric boundary layer by accounting for aerodynamic roughness in the parameterization of surface scalar exchange over sea ice. *Journal of Advances in Modeling Earth Systems*, 15, e2022MS003305.

Goessling, H.F., Tietsche, S., Day, J.J., Hawkins, E. & Jung, T. (2016) Predictability of the Arctic sea ice edge. *Geophysical Research Letters*, 43, 1642–1650.

Graham, R.M., Rinke, A., Cohen, L., Hudson, S.R., Walden, V.P., Granskog, M.A. et al. (2017) A comparison of the two Arctic atmospheric winter states observed during N-ICE2015 and SHEBA. *Journal of Geophysical Research – Atmospheres*, 122, 5716–5737.

Guemas, V., Blanchard-Wrigglesworth, E., Chevallier, M., Day, J.J., Déqué, M., Doblas-Reyes, F.J. et al. (2016) A review on Arctic sea-ice predictability and prediction on seasonal to decadal time-scales. *Quarterly Journal of the Royal Meteorological Society*, 142, 546–561.

Hersbach, H., Bell, B., Berrisford, P., Hirahara, S., Horányi, A., Muñoz-Sabater, J. et al. (2017) Complete ERA5 from 1940: Fifth generation of ECMWF atmospheric reanalyses of the global climate. Copernicus Climate Change Service (C3S) Data Store (CDS).

Hersbach, H., Bell, B., Berrisford, P., Hirahara, S., Horányi, A., Muñoz-Sabater, J. et al. (2020) The ERA5 global reanalysis. *Quarterly Journal of the Royal Meteorological Society*, 146, 1999–2049.

Hodges, K. (1994) A general method for tracking analysis and its application to meteorological data. *Monthly Weather Review*, 122, 2573–2586.

Hodges, K. (1995) Feature tracking on the unit sphere. *Monthly Weather Review*, 123, 3458–3465.

Hodges, K. (2021) TRACK tracking and analysis system for weather, climate and ocean data. Gitlab. https://gitlab.act.reading.ac.uk/track/track

Keeley, S. & Mogensen, K. (2018) Dynamic sea ice in the IFS. *ECMWF Newsletter*, 156, 23–29.

Liu, A., Moore, G., Tsuboki, K. & Renfrew, I. (2006) The effect of the sea-ice zone on the development of boundary-layer roll clouds during cold air outbreaks. *Boundary-Layer Meteorology*, 118, 557–581.

Lüpkes, C. & Birnbaum, G. (2005) Surface drag in the Arctic marginal sea-ice zone: a comparison of different parameterisation concepts. *Boundary-Layer Meteorology*, 117, 179–211.

McGraw, M.C., Blanchard-Wrigglesworth, E., Clancy, R.P. & Bitz, C.M. (2022) Understanding the forecast skill of rapid Arctic sea ice loss on subseasonal time scales. *Journal of Climate*, 35, 1179–1196.

Meier, W.N. & Stroeve, J. (2022) An updated assessment of the changing Arctic sea ice cover. *Oceanography*, 35, 10–19.

Mohammadi-Aragh, M., Goessling, H., Losch, M., Hutter, N. & Jung, T. (2018) Predictability of Arctic sea ice on weather time scales. *Scientific Reports*, 8, 6514.

Notz, D. (2012) Challenges in simulating sea ice in earth system models. *Wiley Interdisciplinary Reviews: Climate Change*, 3, 509–526.

Pedregosa, F., Varoquaux, G., Gramfort, A., Michel, V., Thirion, B., Grisel, O. et al. (2011) Scikit-learn: machine learning in python. *Journal of Machine Learning Research*, 12, 2825–2830.

Pellerin, P., Ritchie, H., Saucier, F.J., Roy, F., Desjardins, S., Valin, M. et al. (2004) Impact of a two-way coupling between an atmospheric and an ocean-ice model over the Gulf of St. *Lawrence Monthly Weather Review*, 132, 1379–1398.

Peng, L., Zhang, X., Kim, J.-H., Cho, K.-H., Kim, B.-M., Wang, Z. et al. (2021) Role of intense Arctic storm in accelerating summer sea ice melt: an in situ observational study. *Geophysical Research Letters*, 48, e2021GL092714.

Peterson, K.A., Smith, G.C., Lemieux, J.-F., Roy, F., Buehner, M., Caya, A. et al. (2022) Understanding sources of northern hemisphere uncertainty and forecast error in a medium-range coupled ensemble sea-ice prediction system. *Quarterly Journal of the Royal Meteorological Society*, 148, 2877–2902.

Pithan, F., Svensson, G., Caballero, R., Chechin, D., Cronin, T.W., Ekman, A.M. et al. (2018) Role of air-mass transformations in exchange between the Arctic and mid-latitudes. *Nature Geoscience*, 11, 805–812.

Rantanen, M., Karpechko, A.Y., Lipponen, A., Nordling, K., Hyvärinen, O., Ruosteenoja, K. et al. (2022) The Arctic has warmed nearly four times faster than the globe since 1979. *Communications Earth & Environment*, 3, 168.

Renfrew, I.A., Elvidge, A.D. & Edwards, J.M. (2019) Atmospheric sensitivity to marginal-ice-zone drag: local and global responses. *Quarterly Journal of the Royal Meteorological Society*, 145, 1165–1179.

Renfrew, I.A. & Moore, G. (1999) An extreme cold-air outbreak over the Labrador Sea: roll vortices and air–sea interaction. *Monthly Weather Review*, 127, 2379–2394.

Rolph, R.J., Feltham, D.L. & Schröder, D. (2020) Changes of the Arctic marginal ice zone during the satellite era. *The Cryosphere*, 14, 1971–1984.

Screen, J.A. (2013) Influence of Arctic sea ice on European summer precipitation. *Environmental Research Letters*, 8, 044015.

Simmonds, I. & Rudeva, I. (2012) *The great Arctic cyclone of august 2012*. Res. Lett: Geophys, p. 39.

Smith, G.C., Bélanger, J.-M., Roy, F., Pellerin, P., Ritchie, H., Onu, K. et al. (2018) Impact of coupling with an ice–ocean model on global medium-range nwp forecast skill. *Monthly Weather Review*, 146, 1157–1180.

Smith, G.C., Roy, F. & Brasnett, B. (2013) Evaluation of an operational ice–ocean analysis and forecasting system for the Gulf of St Lawrence. *Quarterly Journal of the Royal Meteorological Society*, 139, 419–433.

Spensberger, C. & Spengler, T. (2021) Sensitivity of air-sea heat exchange in cold-air outbreaks to model resolution and sea-ice distribution. *Journal of Geophysical Research – Atmospheres*, 126, e2020JD033610.

Srivastava, P., Brooks, I.M., Prytherch, J., Salisbury, D.J., Elvidge, A.D., Renfrew, I.A. et al. (2022) Ship-based estimates of momentum transfer coefficient over sea ice and recommendations for its parameterization. *Atmospheric Chemistry and Physics*, 22, 4763–4778.

Stephenson, S.R., Smith, L.C. & Agnew, J.A. (2011) Divergent long-term trajectories of human access to the Arctic. *Nature Climate Change*, 1, 156–160.

Stern, D.P., Doyle, J.D., Barton, N.P., Finocchio, P.M., Komaromi, W.A. & Metzger, E.J. (2020) The impact of an intense cyclone on short-term sea ice loss in a fully coupled atmosphere-ocean-ice model. *Geophysical Research Letters*, 47, e2019GL085580.

Strong, C. & Rigor, I.G. (2013) Arctic marginal ice zone trending wider in summer and narrower in winter. *Geophysical Research Letters*, 40, 4864–4868.

Tjernström, M., Shupe, M.D., Brooks, I.M., Achtert, P., Prytherch, J. & Sedlar, J. (2019) Arctic summer airmass transformation, surface inversions, and the surface energy budget. *Journal of Climate*, 32, 769–789.

Tjernström, M., Svensson, G., Magnusson, L., Brooks, I.M., Prytherch, J., Vüllers, J. et al. (2021) Central Arctic weather forecasting: confronting the ECMWF IFS with observations from the Arctic Ocean 2018 expedition. *Quarterly Journal of the Royal Meteorological Society*, 147, 1278–1299.

Wang, C., Graham, R.M., Wang, K., Gerland, S. & Granskog, M.A. (2019) Comparison of ERA5 and ERA-interim near-surface air temperature, snowfall and precipitation over Arctic sea ice: effects on sea ice thermodynamics and evolution. *The Cryosphere*, 13, 1661–1679.

Wang, Z., Walsh, J., Szymborski, S. & Peng, M. (2020) Rapid Arctic sea ice loss on the synoptic time scale and related atmospheric circulation anomalies. *Journal of Climate*, 33, 1597–1617.

Wesslén, C., Tjernström, M., Bromwich, D., De Boer, G., Ekman, A.M., Bai, L.-S. et al. (2014) The Arctic summer atmosphere: an evaluation of reanalyses using ASCOS data. *Atmospheric Chemistry and Physics*, 14, 2605–2624.

Xiu, Y., Luo, H., Yang, Q., Tietsche, S., Day, J. & Chen, D. (2022) The challenge of Arctic sea ice thickness prediction by ECMWF on subseasonal time scales. *Geophysical Research Letters*, 49, e2021GL097476.

Zampieri, L., Goessling, H.F. & Jung, T. (2018) Bright prospects for Arctic sea ice prediction on subseasonal time scales. *Geophysical Research Letters*, 45, 9731–9738.

Zuo, H., Balmaseda, M.A., Tietsche, S., Mogensen, K. & Mayer, M. (2019) The ECMWF operational ensemble reanalysis–analysis system for ocean and sea ice: a description of the system and assessment. *Ocean Science*, 15, 779–808.

How to cite this article: Croad, H.L., Keeley, S.P.E., Methven, J., Harvey, B. & Volonté, A. (2025) Examining the sensitivity of ECMWF IFS weather forecasts to sea-ice coupling for the summer-time Arctic and cyclones. *Quarterly Journal of the Royal Meteorological Society*, 1–19. Available from: https://doi.org/10.1002/qj.4899